Alma Mater Studiorum – Università di Bologna

DOTTORATO DI RICERCA IN

Scienze Biotecnologiche e Farmaceutiche

Ciclo XXXI

Settore Concorsuale: 05/E1

Settore Scientifico Disciplinare: BIO12

ANALYSIS OF INTRACELLULAR Zn-HYDROXYAPATITE NUCLEATION IN THE EARLY STAGES OF HUMAN OSTEOGENIC DIFFERENTIATION COMBINING SYNCHROTRON-BASED AND DIFFRACTION TECHNIQUES

Presentata da: Alessandra Procopio

Coordinatore Dottorato

Prof. Santi Mario Spampinato

Supervisore

Dr. Emil Malucelli

Esame finale anno 2019

Abstract

The core knowledge about biomineralization is provided by studies on the advanced phases of the process mainly occurring in the extracellular matrix. This PhD project is based on the analysis of the early stages of biomineralization by evaluating the chemical fingerprint of the initial mineral nuclei deposition in the intracellular milieu and their evolution toward hexagonal hydroxyapatite. The study is conducted on human bone mesenchymal stem cells (bMSC) exposed to an osteogenic cocktail for 4 and 10 days, exploiting laboratory X-ray diffraction techniques and cutting-edge developments of synchrotron based 2D and 3D cryo X-ray microscopy. The synchrotron-based phase contrast imaging revealed few small intracellular depositions @4^{th} day of differentiation and a lot of extracellular and intracellular mineral nuclei @10^{th} day. The 3D reconstructions of phase-contrast images of bMSC at 10 days allowed browsing the entire cell along its thickness to explore the three-dimensional localization of the mineral depositions. Several spots are localized in the cytoplasm of the cell, indicating that the biomineralization starts in the intracellular environment. Synchrotron X-ray Fluorescence Microscopy was carried out to determine the chemical composition of mineral nuclei formation at nanoscale, confirming that mineral accumulation starts early during the osteogenic differentiation of bMSC and providing experimental evidence about the Zn role in HA nucleation. The X-ray fluorescence tomography was performed to obtain the 3D visualization of Ca, P and Zn elemental distribution.

Wide/Small Angle X-ray Scattering and X-ray Absorption Near-Edge Spectroscopy revealed the hexagonal HA as the unique crystalline structure present in differentiating bMSC.

In conclusion, thanks to the combination of 3D high-resolution synchrotron-based X-ray techniques, it has been demonstrated that biomineralization starts with hydroxyapatite nucleation in the intracellular environment, rapidly evolving toward a hexagonal hydroxyapatite crystal very similar to the one present in human bone as detected after just ten days of osteogenic induction.

List of contents

List of abbreviations 8

1. Introduction 9

1.1 State of the art 9

1.2 Bone tissue 11

1.2.1 Histology 12

1.2.2 Biomineralization process 15

1.2.3 Hydroxyapatite 16

1.3 New light to study cell structures and mechanisms 17

1.4 The synchrotron 18

1.4.1 Brightness, brilliance and flux 21

1.5 Synchrotron-based techniques 25

1.5.1 X-ray Fluorescence Microscopy 25

1.5.2 Phase contrast imaging 28

1.5.3 X-ray Absorption Spectroscopy 30

1.5.4 X Ray Absorption Near Edge Structure (XANES) 32

1.6 Small Angle X-ray Scattering (SAXS): a scattering technique ... 33

1.7 Wide Angle X-ray Scattering (WAXS): a diffraction technique . 35

2. AIM of the project 37

3. Materials and Methods.....38

3.1 Isolation and culture of human Mesenchymal Stem Cells.....38

3.2 Osteogenic differentiation of bMSC.....38

3.3 Gene Expression Analysis.....39

3.4 X-ray synchrotron-based fluorescence microscopy and phase contrast imaging.....40

3.4.1 2D and 3D Phase contrast imaging.....41

3.4.2 2D and 3D X-ray fluorescence microscopy.....45

3.3 X-ray absorption near-edge spectroscopy (XANES).....48

3.4 X-ray diffraction techniques: Small/Wide Angle X-ray Scattering 57

3.5 Samples preparation for Synchrotron-based techniques.....60

3.6 Samples preparation for diffraction techniques.....63

4. Results and Discussion.....64

4.1 Osteogenic differentiation and Gene Expression Evaluation.....64

4.2 Electron density and chemical composition of mineral nuclei....67

4.2.1 2D phase contrast imaging.....67

4.2.2 X-ray phase contrast nano-tomography.....70

4.2.3 2D X-ray fluorescence microscopy.....74

4.2.4 X-ray Fluorescence Tomography.....80

4.3 Crystalline structure of mineral nuclei analyzed by X-ray spectroscopy and diffraction.....82

4.3.1 X-ray absorption near edge structure (XANES) spectro-microscopy 82
4.3.2 Small and Wide-angle X-ray scattering 85

5. Conclusions.....89

References.....91

List of abbreviations

BM	Biomineralization
BMP	Bone Morphogenetic Proteins
bMSCs	bone Marrow Mesenchymal Stem Cells
CM	Control Medium
ESRF	European Synchrotron Radiation Facility
EXAFS	Extended X Ray Absorption Spectroscopy Fine Structure
HA	HydroxyApatite
I.D.	Insertion Devices
I.P.	Image Plate
MSCs	Mesenchymal Stem Cells
OM	Osteogenic Medium
RF	Radio Frequency
ROI	Region of Interest
SAXS	Small Angle X-ray Scattering
SR	Synchrotron Radiation
XANES	X Ray Absorption Near Edge Structure
XAS	X-ray Absorption Spectroscopy
XRFM	X-ray Fluorescence Microscopy
XRD	X-ray Diffraction
XMI-L@b	X-ray MicroImaging Laboratory
WAXS	Wide-Angle X-ray Scattering

1. Introduction

1.1 State of the art

The phenomenon of bone regeneration is a widely studied topic due to its effects in the medical, bio-technological and bioengineering fields. In the past two decades, significant progress has been carried out in the field of biomaterials and cell therapy, leading to significant advances in the development of engineered tissues.

Bone tissue engineering represents a novel approach aiming at enhancing bone repair and regeneration (*1*) joining the skills of different specialists (i.e. engineers, surgeons, biologists) in order to define standard protocols useful for a clinical use.

Only the full comprehension of the morphology and functionally of the bone tissue will provide the opportunities to mimic nature for the development of bio-inspired materials and find novel therapeutic approaches to treat diseases such as: osteoporosis and osteoarthritis.

It is known that bone, as well as other biomineralized tissues, shows a complex structure organized on multiple length scales, from the molecular to the macroscopic level (Figure 1.1).

Biomineralization (BM) is the fundamental process in bone formation, modelling and repair (*2*) and it takes place at different spatial and temporal scales.

The early steps of this process occur at the nanometric scale, when, through chemical reactions, orchestrated by the cells, ions in solution are converted

into complex Calcium (Ca)-composite materials (*3–5*), thus forming organized bone mineral crystals of hydroxyapatite (HA).

At the cellular level, the formation, maintenance, and repair of bone are based on the complex crosstalk between osteoclasts, osteoblasts and osteocytes. Osteoblasts differentiate from bone marrow mesenchymal stem cells (bMSC) and stimulate bone formation and calcification until they get embedded in their own matrix and convert into osteocytes.

One of the research goals in studying biomineralization is to understand the mechanisms that organisms use to control mineral formation.

However, all the body of knowledge is provided by studies on the advanced phases of biomineralization, which mainly occur in the extracellular matrix, while studies on the early stages of this process are scarce.

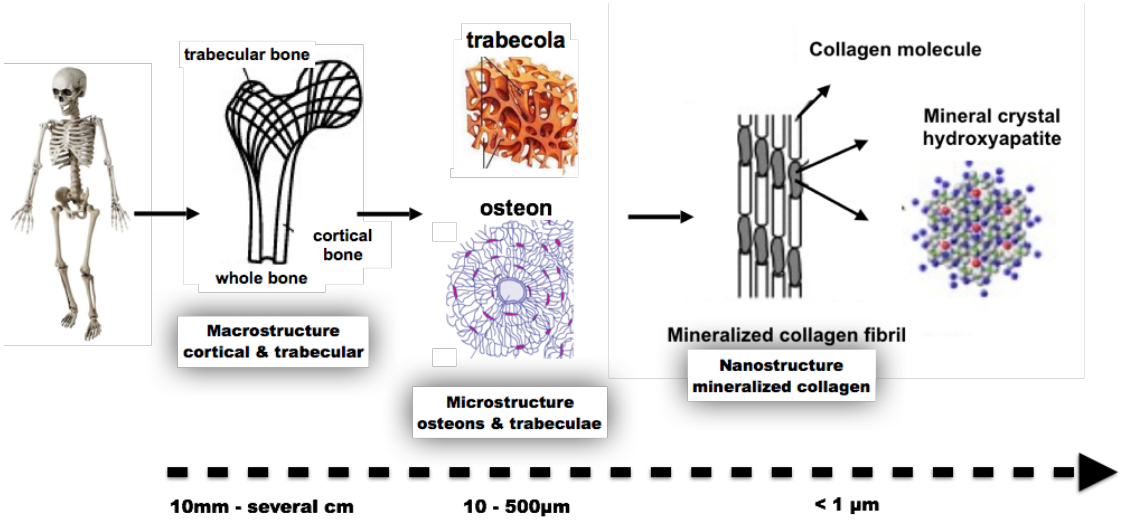

Figure 1.1 - The complex hierarchical and structural organization of bone tissue: at a macrometric scale, the subdivision of cortical and trabecular bone; at micrometric scale, the study of osteon (functional unit of cortical bone) and trabecula (the functional unit of trabecular bone); at nanometric scale, the characterization of mineralized collagen fibril, formed thanks to biomineralization process.

1.2 Bone tissue

Bone tissue belongs to connective tissue classes and it is a composite material, responsible for the mechanical support of the human body and motor regulation, together with the muscular system (*6*).

An overview of the basic functions and characteristics of the bone tissue is essential to design and create biomimetic materials and to treat diseases such as osteoporosis and osteoarthritis. The structure and the composition of this tissue make it both rigid and tenacious. Structurally, it consists of a

mixture of collagen, soft but resistant, and a very rigid but fragile material (hydroxyapatite). Neither component would be able to satisfy by itself the request of a good rigidity coupled with a high tenacity (*7*). The arrangement of the collagen fibrils in the hydroxyapatite matrix gives the bone extraordinary mechanical performances that cannot be reproduced with any homogeneous and isotropic material. The bone matrix is constituted for about 70% of its weight, from inorganic salts of calcium-phosphate nature, present in the form of crystals of hydroxyapatite. Of the remaining 30%, 23% consists of collagen fibrils and water and the remainder from cells, proteoglycans and non-collagen proteins.

1.2.1 Histology

Bone tissue is a metabolically active tissue composed by intercellular substance and several types of cells (cellular component) (*6*).

The first one includes collagen fibrils and various classes of macromolecules such as: proteoglycans, glycoproteins, sialoproteins, osteonectin, fibronectin, alkaline phosphatase, all involved in the mineralization process.

The cellular component of the bone tissue consists of osteoprogenitor cells, osteoblasts, osteocytes and osteoclasts. Bone cells, synergistically, regulate continuous tissue remodelling, repair and regeneration. Essential is also the contribution of endothelial cells in providing, with angiogenesis, the contribution of nutrients and oxygen necessary for the metabolism and the

removal of the products of cell catabolism. The *osteoblasts* are responsible for the synthesis of the bone extracellular matrix and its mineralization. During the ossification process, they form calcium salts around themselves, then they become osteocytes, with a consequent reduction in their metabolic activity. The *osteocytes* are the cell population within the bone tissue; they remain closed in the so-called bone gap and represent a quiescent state of bone cells, but actively act on metabolism. The *osteoclasts* are responsible for bone resorption. The osteoprogenitor cells (pre-osteoblasts), the osteoblasts and the osteocytes are consecutive functional phases of the osteogenic differentiated form *mesenchymal stem cells* (MSCs) (Figure 1.2).

MSCs are a group of clonogenic cells present among the bone marrow stroma and capable of multi-lineage differentiation into mesoderm-type cells such as osteoblasts. Due to their ease of isolation and their differentiation potential, MSC are being introduced into clinical medicine in a variety of applications (*8*). Indeed, it is possible to exploit the possibility of "directing" stem cells towards osteogenic differentiation. This differentiation is obtained by treating mesenchymal stem cells with an osteogenic cocktail (β-glycerophosphate, ascorbic acid and vitamin D). Under these conditions, the cultured cells form aggregates, increasing their production of alkaline phosphatase almost 10 times, and begin to accumulate more and more calcium.

The increased production of calcium successively involves the extracellular matrix deposition of mineralized hydroxyapatite and the expression of osteogenic markers such as osteopontin, osteocalcin and type I collagen.

MSCs can also be induced to differentiate into osteoblasts by the administration of growth factors, such as BMP (Bone Morphogenetic Proteins).

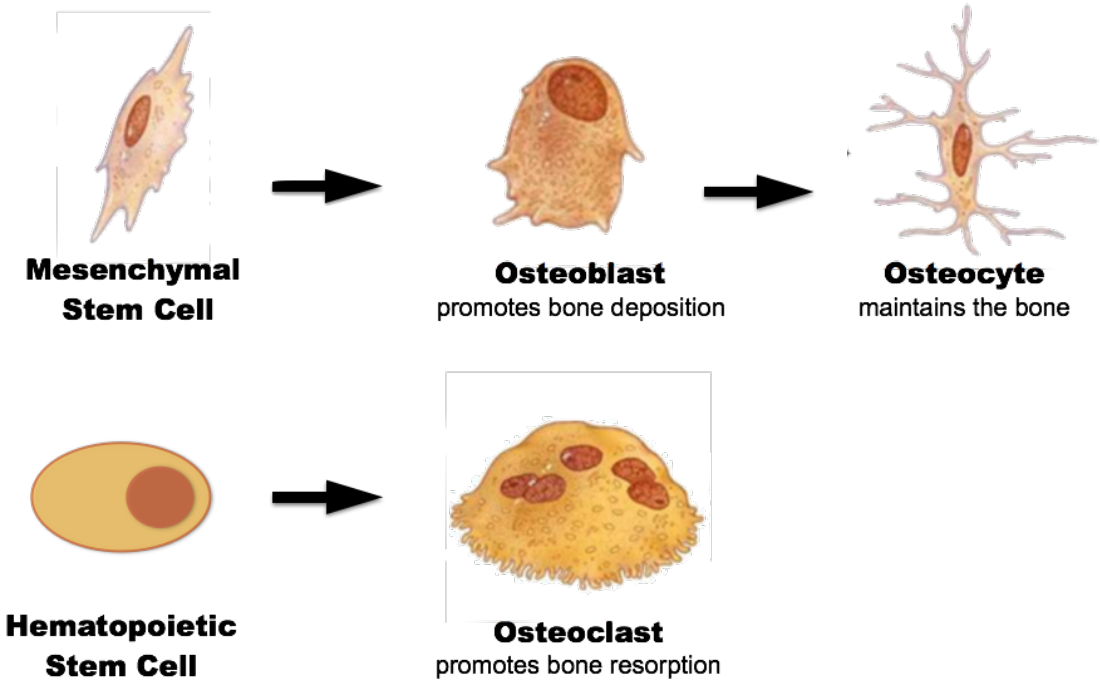

Figure 1.2 – The outline sums up the role and the origin of the cells, which compose the bone tissue.

1.2.2 Biomineralization process

Biomineralization is a widespread and fascinating process that leads to the formation of complex hierarchically structure of the bone. There are many studies at the nanometric scale showing that the highly specialized organic matrix of collagen microfibrils seems to direct the formation of nanosized hydroxyapatite (HA) depositions (*3*, *9–13*). Specifically, the organic component (collagen) is the nucleation site of the mineral phase. At the nanometric scale, the formation of apatitic crystals on collagen fibrils begins in the regions where the fibril has a lower density, the so-called "hole zone". This calcification process, also intended as a process of maturation of the bone tissue, begins at the same time in several distinct nucleation sites leading to a distribution of several crystals, formed in several zones with lower density within single fibrils, separated from each other by regions not mineralized. This means that every single and unidirectional fibril represents an independent nucleation site. The crystals grow parallel to the collagen fibril, in which they are placed, and the result of the process is a mineralized fibril of collagen, which is the basic building element of the bone.

As the mineralization process proceeds, the immature bone changes from a soft, flexible material to a dense, hard and tenacious solid with mechanical properties comparable to metals.

1.2.3 Hydroxyapatite

There are substantial differences between the features of stoichiometric and biological hydroxyapatite, both in terms of crystal structure and composition.

Biological hydroxyapatite is not an inert material: it is part of the complex bone metabolism and is therefore a material in continuous remodelling.

While the hydroxyapatite ($Ca_5(PO_4)_3(OH)$) stoichiometric structure (*14*, *15*) consists solely of Ca, PO_4 and OH groups, the biological one also contains variable amounts of other ions (*16*), which may become part of the crystalline structure as a result of ionic substitutions or, more simply, be adsorbed on its surface. The incorporation of ions different from Ca into the HA structure may alter a number of structural and chemical-physical parameters of the apatite, such as: reticular constants, morphology and crystallite dimensions, crystallinity, thermal stability and solubility,

Bone mineral contains several ionic substitutions such as: sodium (Na), zinc (Zn), magnesium (Mg), iron (Fe) and carbonate (CO_3^{2-}) and so on. These substitutions play a role in influencing the dissolution rate of apatite, which may favour osteointegration (*17*).

Among these ions, Zn is an essential trace element and it has drawn considerable attention due to promote bone formation and to suppress bone resorption (*18*). For this reason, the Zn substitution in the hydroxyapatite structure is most interesting in biomineralization process.

Several studies showed how the Ca-compounds nucleate and grow within an organic matrix, mainly constituted by collagen, which drives the

nucleation site of the mineral phase (*11–13*). However, all this body of knowledge is provided by studies on the advanced phases of biomineralization, which mainly occur in the extracellular matrix, while studies on the early stages of this process are scarce. Specifically, the accumulation of early hydroxyapatite crystals and the transport of early mineral to the extracellular matrix space are incompletely understood (*19*).

1.3 New light to study cell structures and mechanisms

Nowadays new powerful and unconventional techniques based on synchrotron light are used to analyze biological samples, with the aim of clarifying their structure at the sub-micrometric level and in this way discovering pathophysiological functions not completely known.

Synchrotron light has many advantages, which make it much more powerful for some biological applications than laboratory-based source (*20*).

The biological systems contain an ensemble of cells with heterogeneous chemistry and elemental content; therefore single cell analysis represents a suitable strategy to achieve an accurate characterization of these kinds of samples (*21*) .

The synchrotron-based techniques allow the analysis of single cells, contributing to elucidate the distribution, concentration and chemical state of metals inside tissues and cells at the organelle level.

This contribution is not only highly challenging but represents important objectives in modern analytical chemistry and an essential step towards the

precise understanding of some cellular pathophysiological or toxicological processes.

1.4 Synchrotron radiation

When electrons or positrons moving at relativistic speed, i.e., close to the velocity of light, if they are subjected to a magnetic field, their trajectory follows a circular orbit and synchrotron radiation (SR) is emitted in the tangential direction. The radiated energy is proportional to the fourth power of the particle speed and inversely proportional to the square of the radius of the path. The beam is concentrated into a forward narrow cone with half angle of typically 0.1 to 1 mrad. Synchrotron radiation facilities typically consist of an injection system, a storage ring and beamlines. In the injection system, electrons are generated, pre-accelerated, and sometimes a second accelerator further accelerates these electrons to few GeV before injection into the storage ring.

In the ring, bunches of electrons periodically circulate at relativistic speed for periods up to many hours. The storage ring consists of radio frequency (RF) cavities, bending magnets, insertion devices and different control systems mainly to control the orbit of the electrons (Figure 1.3).

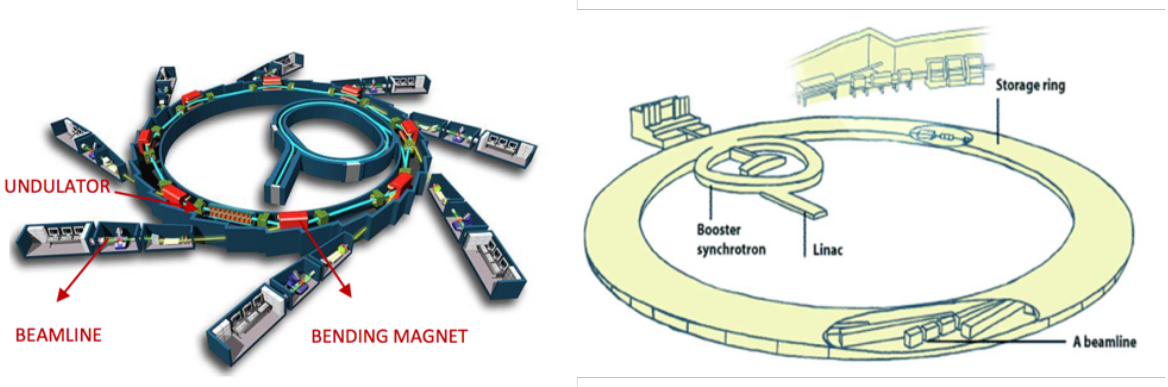

Figure 1.3 - Schematic picture of the synchrotron ring of the ESRF (up) and more detailed view (bottom). Electrons are first accelerated in the linear accelerator (linac) and in a booster synchrotron, and then they are injected into a storage ring.

The RF cavity system restores energy, which the electrons loose because of the emission of SR, and stabilizes the bunch of electrons. The high-energy electrons are maintained in a planar orbit by using bending magnet.

Any accelerated charge radiates an electromagnetic field which, if the particle has a speed v << c (c light speed), is isotropic around the acceleration.

For a relativistic effect, when the speed of the emitting electrons increases to relativistic values (v ≈ c) the radiation pattern is compressed into a narrow cone in the direction of motion, resulting into an emission tangential to the particle orbit. The vertical half-opening angle, ψ, is given by(*22*):

$$\psi \approx \frac{mc^2}{E} \approx \gamma^{-1} \qquad (1.1)$$

For electrons or positrons of energy E expressed in GeV γ = 1957 * E. Thus for a storage ring of $E = 1\ GeV$ it follows that $\gamma \approx 80\ mrad$.

The emission spectrum is continuous from infrared radiation up to a critical wavelength λ_c, which depends on ρ and γ. The critical wavelength is defined as the value for which half of the total power is emitted at wavelengths shorter than the critical one; λ_c is given by:

$$\lambda_c = \left(\frac{4\pi}{3}\right)\frac{\rho}{\gamma^3} \qquad (1.2)$$

In order to improve the intensity of emission, insertion devices (I.D.) have been conceived where the charged particles pass through several magnetic dipoles (Figure 1.4) and are therefore compelled to have a zigzag trajectory. At each wiggler (Figure 1.4), they emit radiation, which is therefore enhanced, of a 2N factor where N is the number of poles. These devices are called wigglers or undulators and the distinction is essentially due to the relation between the angular deviation α at each wiggler and the aperture γ^{-1}. Values of $\alpha \gg \gamma^{-1}$ identify wigglers, while $\alpha\gamma^{-1}$ identify undulators.

The radiation emitted by a wiggler is the incoherent sum of the radiation fields emitted by each individual magnet. The spectrum is continuous but shifted at higher energies with respect to that of a bending magnet. Instead, in the undulator regime, the amplitudes of the field radiated at each period

of the particle trajectory may interfere resulting in a periodic radiation field. The spectrum is thus not continuous, but resonances occur at given frequencies (the fundamental and the harmonics).

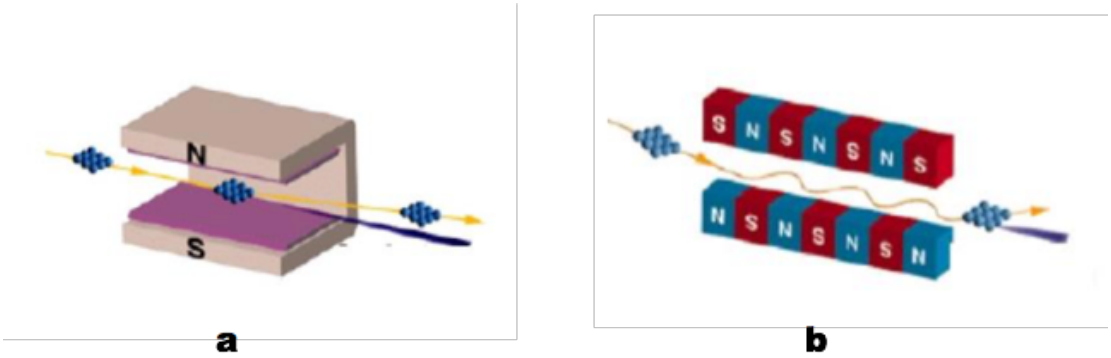

Figure 1.4 - a) Schematic picture of Bending Magnet. b) Schematic picture of Wiggler.

1.4.1 Brightness, brilliance and flux

The flux in a given band-pass energy is defined as:

$$F = \frac{Photons}{s} / \frac{\Delta\lambda}{\lambda} \qquad (1.3)$$

Taking into account also the angular aperture (i.e. the collimation), we can speak of brightness which is the flux per solid angle (*22*):

$$Brightness = 10^{16} \frac{Photons}{s \cdot mm^2 mr^2 (0.1\ \%\ BW)} \qquad (1.4)$$

In fact also the size source is of importance and therefore the brilliance becomes the parameter of interest:

$$Brilliance = Brightness/\sigma_x \sigma_y = \frac{ph/s/mrad^2/\sigma_x \sigma_y}{(\Delta\lambda/\lambda)} \qquad (1.5)$$

Where σ_X and σ_Y are the transverse source sizes (horizontal and vertical).

The emittance of the source ε is defined as:

$$\varepsilon = \varepsilon_h * \varepsilon_v \qquad (1.6)$$

Where the horizontal and vertical emittances ε_h and ε_v are defined as:

$$\varepsilon_h = \sigma_x \sigma'_x$$
$$\varepsilon_h = \sigma_y \sigma'_y \quad (1.7)$$

Where σ_x and σ_y are the horizontal and vertical source size respectively and σ'_x and σ'_y are the divergence of the beam in the horizontal and vertical directions respectively. The figures of merit are brilliance and emittance. The first should be as high as possible and the last should be as low as possible. Just to give an idea about numbers, if an X-ray tube has brilliance of the order of 10^7, peak brilliance at an undulator beamline of third generation S.R. can be as high as 10^{20} - 10^{21}. For example, horizontal and vertical emittances at European Synchrotron Radiation Facility (ESRF) reached values as low as 4 and 0.025 nm respectively.

Time structure is also important, at least for time resolved experiments. S.R. is not continuous, but is emitted in bunches corresponding to the electron bunches in the storage ring. Duration of a single bunch is, for ex. at (ESRF) in Grenoble, of 20 ps. Time between bunches depend on the filling mode of the storage ring. For single bunch mode (the one generally used for time resolved experiments) is about 3 μs at ESRF.

One of the important characteristics of the photon beam is the coherence. There are two kinds of coherence: transverse coherence and longitudinal coherence. The transverse coherence refers to the coherence of the electromagnetic disturbances at two points perpendicular to the propagation

direction.

Consider two points P_1 and P_2 that lie on the same wave front of an electromagnetic wave at time t = 0. Let $E_1(t)$ and $E_2(t)$ be the corresponding electric fields at these points. Let's suppose that the difference between the phases of the two fields at t = 0 is zero. If this difference remains zero at any time t > 0, there is a perfect coherence between the two points.

If this occurs for any two points of the electromagnetic wave front, the wave is *perfectly coherent* (the degree of spatial coherence is 1). Usually, for any point P_1, the point P_2 must lie within some finite area (*coherence area or length*) around P_1 to maintain the phase correlation.

From the Van Cittert-Zernike theorem (*23*), it comes out that, the radiation field from a primary incoherent source gains coherence during the propagation. Furthermore, the larger is the distance from the source and the smaller is the source size; the larger is the coherence length.

The coherence length l can therefore be approximately defined as:

$$l = \lambda \ (L/s) \qquad (1.8)$$

Where λ is the wavelength, L the distance source-sample and s the transversal source size. Synchrotron radiation is inherently incoherent, but due the large distance from the source, the beam at the sample position is larger with respect to tabletop laboratory sources.

The longitudinal coherence refers to the case of two points along the propagation direction and is related to the monochromaticity of the beam.

The longitudinal coherence is characterized by the longitudinal coherence length l_c, which is related to the bandwidth $\Delta\lambda/\lambda$ by:

$$l_c = \frac{\lambda^2}{\Delta\lambda} \tag{1.9}$$

1.5 Synchrotron-based techniques

Synchrotron X-rays can be exploited for traditional X-ray imaging, phase-contrast X-ray imaging, and tomography.
It is possible to combine imaging techniques with spectroscopy, such as X-ray fluorescence or X-ray absorption spectroscopy, in order to map a sample's chemical composition or oxidation state with sub-micron resolution (*20*).

1.5.1 X-ray Fluorescence Microscopy

Synchrotron X-ray Fluorescence Microscopy (XRFM) is a powerful technique, which exploits the spectrally pure and finely focused X-ray beam from a synchrotron. In XRFM process, a photon is absorbed by an atom creating a hole in the atom with the ejection of an electron. The energy of this photoelectron is the difference between that of the incident photon and the binding energy of the electron. Electrons cascading in from

outer electron shells fill the electron vacancies created by the incoming photon. These have higher energy states than inner shell electrons, and the rearrangement of electrons results in emission of Auger electrons and of X-ray photons characteristic of the given atom (Figure 1.5).

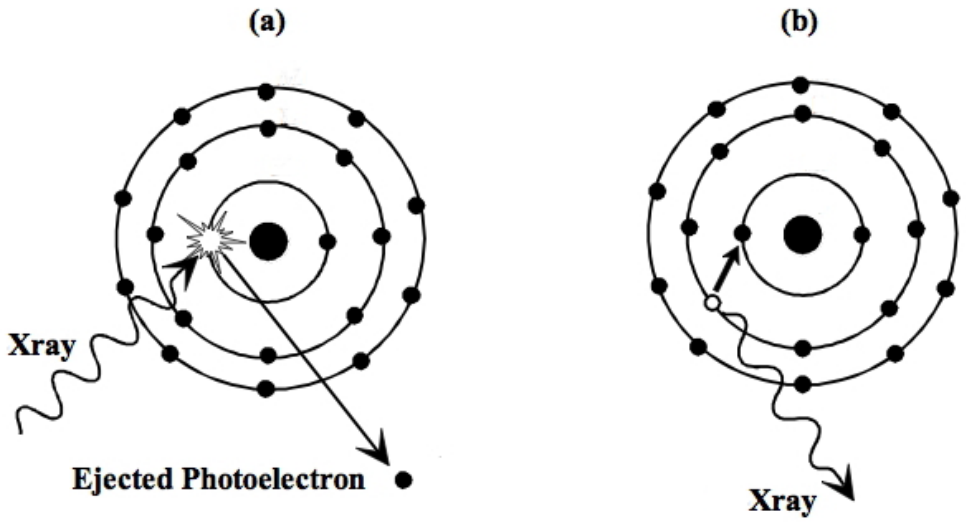

Figure 1.5 - Bohr atom model - a positively charged nucleus surrounded by electrons that move within defined areas (called "shell" or "orbitals") - which illustrate the basic principle of X-ray fluorescence. (a) Excitation with X-ray leads to the ejection of a inner orbital electron from the atom. (b) The generated vacancy is filled by a higher-shell electron, during this process a photon, whose energy is equal to the difference in binding energies of the two shells involved in the transition, is emitted.

Image source: adapted from "PhotoelectricEffect" by Kieranmaher - Own work. Licensed under Public Domain via Wikimedia Commons - https://commons.wikimedia.org/wiki/File:PhotoelectricEffect.jpg#/media/File:PhotoelectricEffect.jpg

This emission of photons is called X-ray fluorescence and it is emitted isotropically. The X-ray fluorescence lines are historically termed by the letter K, L, or M (Figure 1.6), indicating which shell had the original vacancy, and by a subscript alpha (α) or beta (β), which indicates the higher shell from which electrons fill to fill the vacancy and produce the X-ray. For example, a K_α line is produced by a vacancy in the K shell filled by an L shell electron, whereas a K_β line is produced by a vacancy K shell filled by an M shell electron. The K lines are by far the most intense; moreover, the K_α transition is on average 6 to 7 times more intense than the K_β ones. Therefore, the K_α line is in general the choice for quantification purposes. Obviously, to generate K lines the incoming photons must have enough energy to excite the innermost electrons.

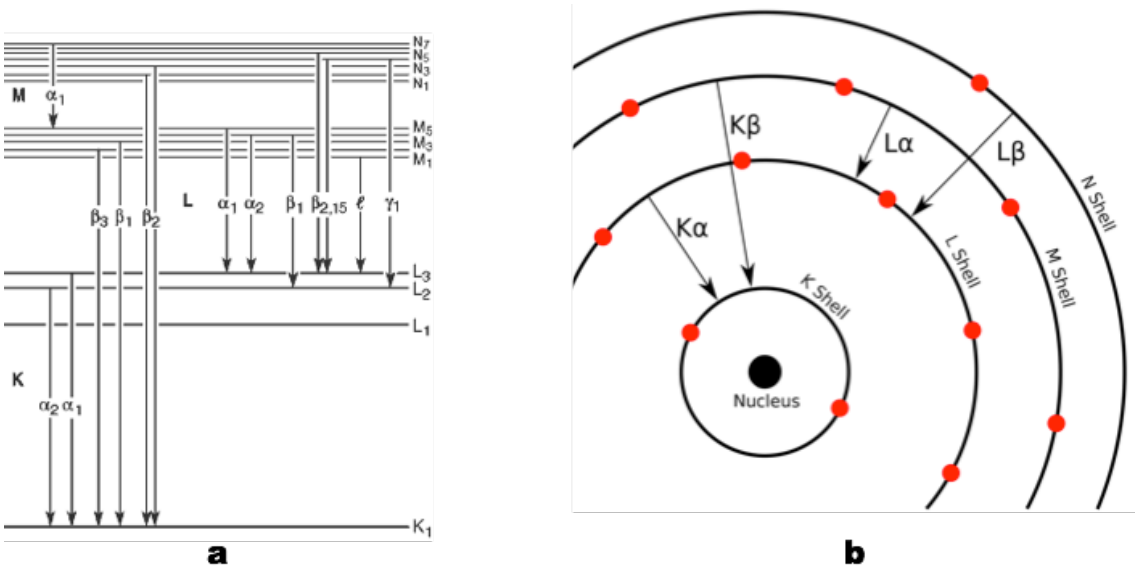

Figure 1.6 - X-ray emission lines. (a) x-ray emission lines described according to the "Siegbahn notation"(*24*). (b) Bohr model of atom which shows K and L emission lines with respect to the orbitals.

Image sources: left image - Thompson AC, Kirz J, Attwood DT, Gullikson EM, et al. X-Ray Data Booklet.. Third edition, september 2009. Thompson AC, editor. Lawrence Berkeley National Laboratory - University of California; Available from: http://cxro.lbl.gov//PDF/X-Ray-Data-Booklet.pdf.. Right image - "CharacteristicRadiation" by English Wikipedia user HenrikMidtiby. Licensed under CC BY-SA 3.0 via Wikimedia Commons - https://commons.wikimedia.org/wiki/File:CharacteristicRadiation.svg#/media/File:CharacteristicRadiation.svg

1.5.2 Phase contrast imaging

When X-rays go through an object, two phenomena can take place, according to the refractive index (*25*):

$$n = 1 - \delta + i\beta \qquad (1.10)$$

The imaginary part of the refractive index β describes the absorption of the X-rays and the image contrast is due to absorption differences and the amplitude of the radiation changes. The real part of the refractive index depicts the delay in passing of the X-rays through the object.

Phase contrast imaging exploits the effects due to the decrement of the real part, δ. The phase shift between the wave transmitted through and outside the object produces a difference in the δ value. The phase shift induced by the object can be described as (*26*):

$$\phi(x,y) = -(\frac{2\pi}{\lambda}) \int \delta(x,y,z)dz \qquad (1.11)$$

Where z is the propagation direction and λ the wavelength.

Generally, absorption radiology is the most common way imaging is working since the X-ray imaging was born. The absorption contrast depends only on the linear absorption coefficient μ and it is independent on the spatial degree of coherence of the beam. Instead, phase contrast imaging such as that based on free space propagation (defocused imaging) requires some degree of coherence of the incident beam. This technique permits to image weak absorbing samples that would not provide enough contrast in absorption. A typical example is biological samples. With the third generation synchrotron radiation sources generating a highly coherent beam, many techniques based on phase imaging have been developed.

The main difficulty in phase contrast imaging is that the phase cannot be measured directly and therefore several indirect methods have been

developed to transform phase modulations into intensity modulations. The principle of the free space propagation phase imaging is that differences in optical path for the beam transmitted through an object are directly converted, after interference, into inhomogeneous intensity, hence contrasts.

1.5.3 X-ray Absorption Spectroscopy

The spectroscopy XAS (X-ray Absorption Spectroscopy) studies the trend of the absorption coefficient of a substance in function of the incident radiation energy in the X-ray region, from an energy that is just lower that the photoelectric absorption threshold till to 1000 eV after the threshold. It allows studying the structure of atoms in molecules and materials. The involved energies, in XAS spectra, range from a few hundred eVs (soft X-rays) to several tens of thousands of eVs (hard X-rays). Since it is necessary to change the radiation energy continuously over a wide range, and since the useful signal is typically one thousand of the total signals, a high-brightness X-ray source is required over a large energy band, i.e. a source of synchrotron light.

The XAS spectrum is conventionally divided into three distinct regions (as shown in Figure 1.7) and different information can be obtained depending on the energy range considered:

- **Pre-edge region**: The energy range is limited to some eV before the absorption threshold. There is the presence of weak discontinuities due to the transitions of the core electron to other bound states.

- **XANES (X Ray Absorption Near Edge Structure)**: the part of the spectrum that extends from 0 to 50 eV above the absorption threshold. The study of XANES, combined with the pre-edge area, provides information on the local geometric and electronic configuration. In other words, it allows gaining information on the chemical bond status between the different atoms of the sample and it is strongly affected by the oxidation state of the photon-absorbing atom.

- **EXAFS (Extended X Ray Absorption Spectroscopy Fine Structure)**: the region of the spectrum that is between 100 eV and 1000 eV beyond the absorption threshold. From the EXAFS analysis, it is possible to determine the chemical state of the sample in the immediate vicinity of the absorptive atom (about ten Angstroms).

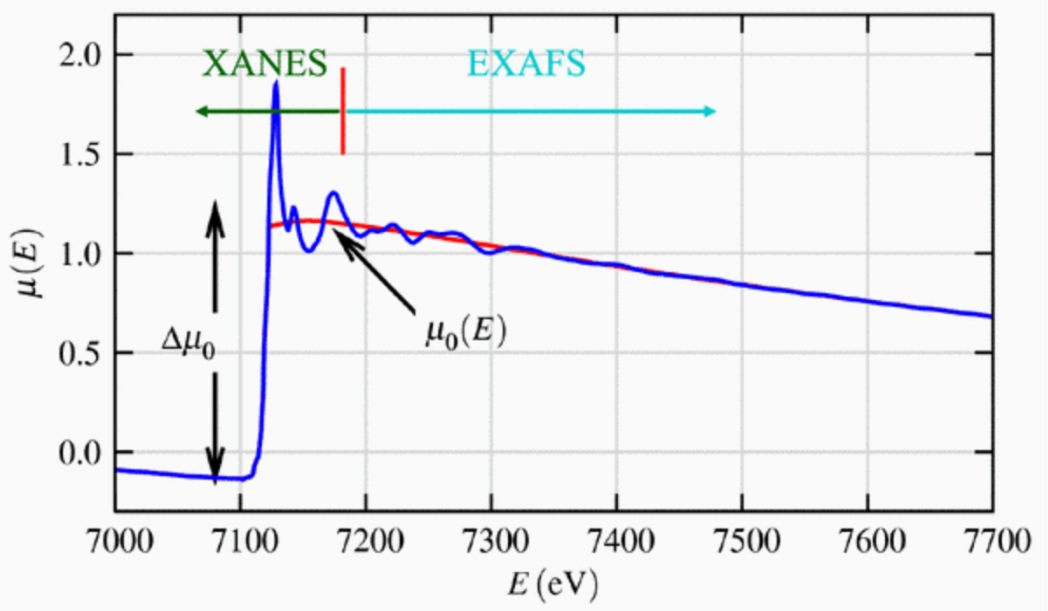

Figure 1.7 - XAS spectra of FeO (blue) showing the XANES and EXAFS regions as well as the edge-step Δμ0(E0) and the smooth background function μ0(E) (red) representing the absorption of an isolated atom.

Image source: http://www.ati.ac.at/index.php?id=247

1.5.4 X Ray Absorption Near Edge Structure (XANES)

XANES spectroscopy is a technique that allows evaluating the electronic, structural and magnetic properties of materials. In this technique, a photon is absorbed and an electron is excited from a core state to an empty state. To excite an electron in a given core-level, the photon energy has to be equal or higher than the binding energy of this core-level. The energy of an absorption edge corresponds to the core-level energy, which is characteristic for each element, making XANES an element-selective technique (*27*).

1.6 Small Angle X-ray Scattering (SAXS): a scattering technique

Two kinds of scattering may take place when a photon interacts with an atom(*28*):

• Incoherent or inelastic or Compton scattering; the change of propagation direction is accompanied with an increase of wavelength and a change of phase.

• Coherent or elastic or Rayleigh scattering; phase and energy are conserved.

The X-rays of a known wavelength interact with an atom and are scattered through an angle θ.

The wavelength of scattered photons is related to θ:

$$\lambda' - \lambda = \frac{h}{m_e c}(1 - cos\theta) \qquad (1.12)$$

Where λ is an initial wavelength, λ' wavelength after scattering, h the Planck constant, m_e the electron rest mass and c is the speed of light.

The probability for Compton scattering increases with increasing photon energy (up to a certain level, then it decreases) and is proportional to

atomic number of the scattering atom. Rayleigh scattering decreases with increasing energy and decreasing atomic number.

Elastic scattering takes place when the incident particles due to interaction with other particles/waves conserve their kinetic energy, while the propagation direction is changed. When considering I_0 as incident particles per unit area per sec., I_s as scattered particles within the solid angle $\Delta\Omega$ and by use of differential scattering cross section $d\sigma/d\Omega$ one can formulate:

$$I_s = I_0 \Delta\Omega \frac{d\sigma}{d\Omega} \tag{1.13}$$

Small-angle X-ray scattering (SAXS) is a scattering technique by which the density differences in a sample can be quantified at nanometric scale. This is achieved by the analysis of the elastic scattering behaviour of X-rays that travell through a material, recording their scattering at small angles (typically 0.1° - 10°). SAXS is typically capable of delivering structural information of dimensions between 1 and 100 nm, and of repeat distances in partially ordered systems of up to 150 nm (*29*).

1.7 Wide Angle X-ray Scattering (WAXS): a diffraction technique

In crystallography, crystal structure describes the ordered arrangement of atoms, ions or molecules in a crystalline material. This crystal structure occurs from the intrinsic nature of the constituent particles to form periodic patterns that repeat identical along the principal directions of three-dimensional space in matter. The smallest group of particles in the material that constitutes the repeating pattern is the unit cell of the structure that defines the symmetry and structure of the entire crystal lattice, which is built up by repetitive translation of the unit cell along its principal axes.

The size of the unit cell and the angles between them vary with the crystalline system (7 are permitted: cubic, tetragonal, orthorhombic, hexagonal, rhombohedral, monoclinic, triclinic) (*30*).

X-ray diffraction (XRD) is a versatile, non-destructive technique that reveals detailed information about the crystallographic structure of materials. When a monochromatic X-ray beam with wavelength λ is projected onto a crystalline material at an angle θ, diffraction occurs only when the distance travelled by the rays reflected from successive planes differs by a complete number n of wavelengths, according to the Bragg's law:

$$n\lambda = 2dsin\theta \qquad (1.14)$$

Where *d* is the distance between atomic layers in a crystal. By varying the angle, the Bragg's Law conditions are satisfied by different d-spacing in polycrystalline materials. Plotting the angular positions and intensities of the resultant diffracted peaks of radiation produces a pattern, which is characteristic of the sample. Where a mixture of different phases is present, the resultant diffractogram is formed by addition of the individual patterns.

Wide-Angle X-ray Scattering (WAXS) is an X-ray diffraction technique used to determine the crystalline structure of a sample. This technique specifically refers to the analysis of Bragg peaks scattered to wide angles ($2\theta > 1°$), which by Bragg's law implies that subnanometer-sized interplanar distances cause them.

2. AIM of the project

In this PhD project, we investigated the early stages of Biomineralization by evaluating the genesis of the initial mineral nuclei depositions and their evolution toward hydroxyapatite, in human bone mesenchymal stem cells, exposed to an osteogenic cocktail for 4 and 10 days.

The PhD project provided an important progress on the knowledge of the molecular events that occur in the initial phases of osteogenesis. It was reveal for the first time in human that the biomineralization starts with hydroxyapatite nucleation within the cell to rapidly evolve towards hexagonal hydroxyapatite crystal very similar to the one present in mature human bone and it was highlight the relevance of Zn in favouring hydroxyapatite nucleation.

To achieve this goal, it was exploited the versatility of X-ray techniques generated by high brilliance synchrotron light, pushing them to their full potentiality, achieving spatial resolutions never obtained before on cells in both two and three dimensions (tomography). In particular, in this study, the 3D phase contrast holographic nano-tomography reconstruction (pixel size 15 nm) allowed to determine the intracellular morphology and the real localization of the mineral nuclei formations. Moreover, for the first time a fluorescence tomography reconstruction was applied in single cell winning the technical challenge, which has so far restricted its application to biological naturally, shielded samples such seeds, grains or diatoms.

3. Materials and Methods

3.1 Isolation and culture of human Mesenchymal Stem Cells

Mesenchymal stem cells from human bone marrow (bMSC) of male healthy volunteers were donated by prof. Berti (Policlinico, Milan). The cells were isolated after obtaining informed consent from all the subjects at the Policlinico in Milano, in compliance with the Helsinki declaration and with applicable laws and regulations, according to institutional guidelines and regulations of the Ehical Committee of "IRCCS Policlinico" Milano. bMSC were tested for purity by flow cytometry and cultured in Dulbecco's Modified Eagle's Medium with 1000 mg/L glucose, 10% FBS and 2 mM L-glutamine (culture medium, CM) at 37°C. When confluent, the cells were detached by treatment with trypsin-EDTA 1X (Sigma-Aldrich), characterized, subcultured, and used at passage numbers 3-5 (*31*).

3.2 Osteogenic differentiation of bMSC

To induce osteogenic differentiation, bMSC were seeded in 6- or 96-well plates. Once the cells were confluent, an osteogenic cocktail was added to the medium (osteogenic medium, OM).

The osteogenic cocktail contains 2 x 10^{-8} M $1_{\alpha,25}$ - Dihydroxyvitamin D3, 10 mM β-glycerolphosphate and 0.05 mM ascorbic acid (Sigma-Aldrich) (*21*). To investigate calcium deposition by bMSC, the cells were rinsed with PBS, fixed (70% ethanol, 1 h) and stained for 10 min with 2% Alizarin Red S (pH 4.2, Sigma-Aldrich) (*32*). The experiment was repeated three times in triplicate. Photographs were taken at 10x magnification. Alizarin Red S staining was released from the cell matrix by incubation in 10% cetylpyridinium chloride (Sigma-Aldrich) in 10 mM sodium phosphate (pH 7.0), for 15 min and the absorbance measured at 562 nm.

3.3 Gene Expression Analysis

Total RNA was extracted by the PureLink RNA Mini kit (Thermo Fisher Scientific). Single-stranded cDNA was synthesized from 0.2 µg RNA in a 20 µL final volume using High Capacity cDNA Reverse Transcription Kit, with RNase inhibitor (Thermo Fisher Scientific) according to the manufacturer's instructions. Real-time PCR was performed three times in triplicate on the 7500 FAST Real Time PCR System instrument using TaqMan Gene Expression Assays (Life Technologies, Thermo Fisher Scientific): Hs00231692_m1 (*RUNX2*), Hs00164004_m1 (*COL1A1*), Hs01587814_g1 (*BGLAP*) and Hs00959010_m1 (*SPP1*).

The housekeeping gene *GAPDH* (Hs99999905_m1) was used as an internal reference gene. Relative changes in gene expression were analyzed by the

2-ΔΔCt method (*32*). The experiments were repeated three times in triplicate.

3.4 X-ray synchrotron-based fluorescence microscopy and phase contrast imaging

The X-ray phase-contrast and X-ray fluorescence measurements were performed at the ID16A-NI 'Nano-Imaging' beamline of the European Synchrotron Radiation Facility (Figure 3.1). The beam was focused using Kirkpatrick-Baez mirrors to a spot measuring 23 nm x 37 nm and the selected energy was 17.05 keV.

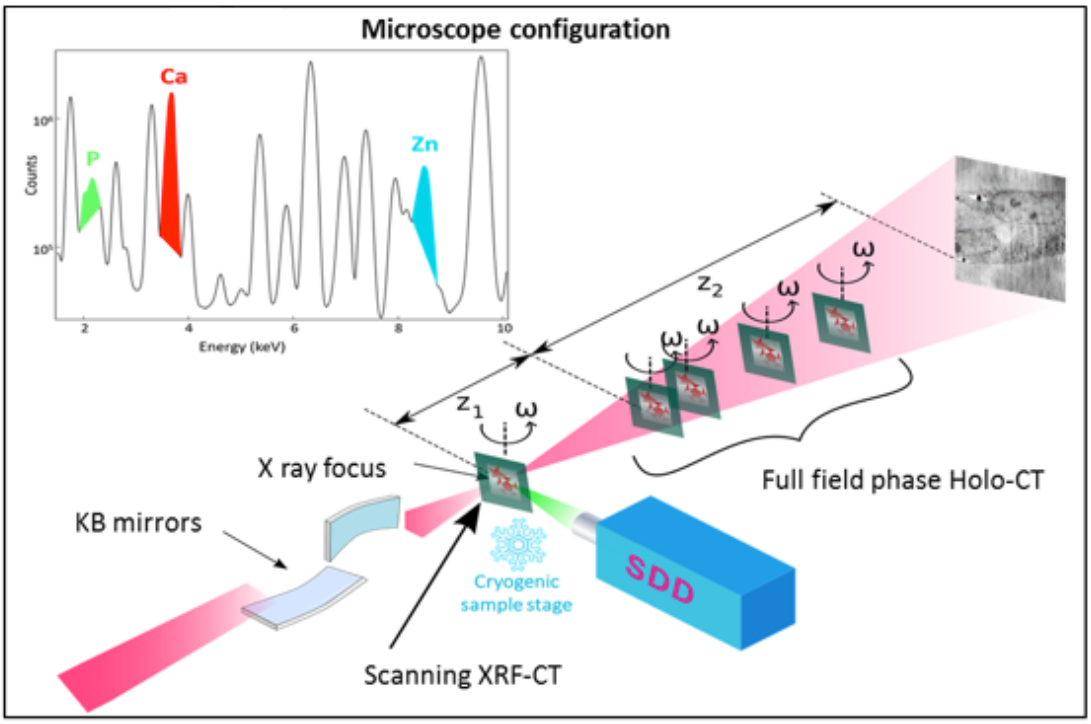

Figure 3.1 - The experimental set-up at the ID16A-NI 'Nano-Imaging' beamline of the ESRF Synchrotron.

3.4.1 2D and 3D Phase contrast imaging

Phase contrast imaging is perfectly suitable for non- or weakly absorbing samples, such as soft biological tissues illuminated by hard X-rays. If they are sufficiently thin, only the phase of the waves transmitted through them will change. With the phase retrieval procedure, it is possible to obtain the spatial distribution of the sample refractive index, in its real and imaginary components, starting from the analysis of the images at the detector. One

can consider phase contrast images as encrypted images of the phase distribution Φ (x, y). The problem of phase retrieval is nothing more than the problem of decoding such images to retrieve the phase Φ (x,y) of the incident radiation, often called as 'inverse problem'. To solve this kind of problem, different approaches exist: the Gerchberg-Saxton algorithm (*33*), the transport-of-intensity equation (TIE) (*34*) and the transfer function approach (*35*). The last one is used in this PhD work for phase contrast imaging of biological samples.

According to this approach, it is convenient to make images at several defocusing distances, in order to reconstruct the phase. In this way, it is possible to optimize the response for all the spatial frequencies, since for each distance a given spatial frequency have maximum phase contrast and it is also avoid "blindness" for some frequency.

In this PhD work, the samples with bMSC after 4 and 10 days of osteogenic differentiation were placed in the cone beam at a distance z1 downstream of the focus. The 2D detector (a FReLoN charged-coupled device with binned 2048 × 2048 pixels array) was placed at a distance z2 downstream of the sample, achieving a magnification:

$$M = \frac{(z1 + z2)}{z1} \qquad (3.1)$$

and an effective propagation distance:

$$D = \frac{z2}{M} \tag{3.2}$$

The magnification was set to achieve a pixel size of 50 nm (sample at 4th day of differentiation), 15 nm and 7 nm (sample at 10th day of differentiation). For phase retrieval, the samples were put at different distances (29 mm, 30 mm, 34 mm and 44 mm) downstream of the X-ray focus resulting in different magnification and defocusing distances. To correct for inhomogeneity in the incoming beam and to subtract the electronic noise, we acquired also darkfields (i.e. acquisitions without beam), and flat field images, i.e. acquisitions with the beam but without the sample. Furthermore, to allow for averaging, we acquired 17 images, 10 reference beams and 20 darkfields for each of the four distances. We take average of the 17 images, then we subtracted the average of the dark field and we normalized with the average of the flat field image (to which we subtracted the average of the dark field). After these procedures, we obtain four images, one for each distance. The final result of the phase retrieval reconstruction is the phase map φ (x,y), that represents the electron density of the samples.

X-ray phase contrast nano-tomography was performed on the samples with bMSC after 4 and 10 days of osteogenic differentiation. The magnification

was set to achieve a pixel size of 50 nm (sample at 4^{th} day of differentiation) and 15 nm (sample at 10^{th} day of differentiation). Tomographic scans were recorded at four different distances from the focal spot. For each scan, 2000 projections over 180 degrees with an exposure time of 0.25 s were recorded. For image reconstruction, each set of four holograms corresponding to one rotation angle was brought to the same magnification and aligned before being introduced into a phase-retrieval algorithm. These steps of data processing are implemented in Octave. The obtained phase maps were then used for tomographic reconstruction via filtered back-projection using PyHST (*39*).

The output of the holographic nano-tomography is set of tilted projections or tomograms.

After this first reconstruction, unfortunately, the projections are affected by missing wedge artifacts. These can be arise from an imprecise projection alignment, from the structural instability of specimens during tomogram acquisition (*38*, *39*).

By simply replacing with zeros the projections affected by missing wedge artifacts one can obtain a better reconstruction.

At the end, 3D renderings were realized through a manual segmentation in Chimera software, to better visualize the 3D information given by the reconstructed electron density.

3.4.2 2D and 3D X-ray fluorescence microscopy

Since the X-ray fluorescence spectrum is characteristic and different for each element, X-ray fluorescence spectroscopy has been used since the discovery of X-rays for elemental analysis. However, only with the advent of third generation synchrotron radiation sources, the X-ray Fluorescence Microscopy (XRFM) could become a technique able to give information at micrometer and sub-micrometer scale. XRFM works in scanning mode. Digital images of the sample at micrometer or nanometer spatial resolution are built, pixel-by-pixel, by scanning the sample through the beam. The resulting X-ray fluorescence spectrum is characteristic of the chemical elements at that pixel. Mathematical deconvolution of the fluorescence spectrum reveals the chemical composition, from which quantitative elemental images of the sample are assembled. One of the most important applications is in the biomedical field. XRFM provides an excellent trace element sensitivity, and, due to the large penetration depth of hard X-rays, an opportunity to image whole cells and quantify elements on a *per cell* basis. Moreover, because specimens prepared for XRFM do not require sectioning, they can be investigated close to their natural, hydrated state with cryogenic approaches (*40–42*).

In this study, for the X-ray fluorescence measurements, the sample was placed in the focal plane and elemental maps were obtained through raster scanning. The selected pixel sizes were 100 nm for non-induced bMSC, 70 nm for the samples measured at 4 days and 10 days of osteogenic differentiation and 15 nm for more precise maps of individual mineral

nuclei at 10th day of differentiation. The photon flux was about $2.3x10^{11}$ photons/sec, the exposure time was 0.05 s per pixel and the recorded maps covered areas of 10-20 μm x 10-20 μm, depending on the cell sizes. For each pixel, the fluorescence spectrum was recorded with an energy resolving silicon drift detector, orthogonal to the incoming beam. A typical spectrum of the bMSC at 4th of differentiation is shown in Figure 3.2.

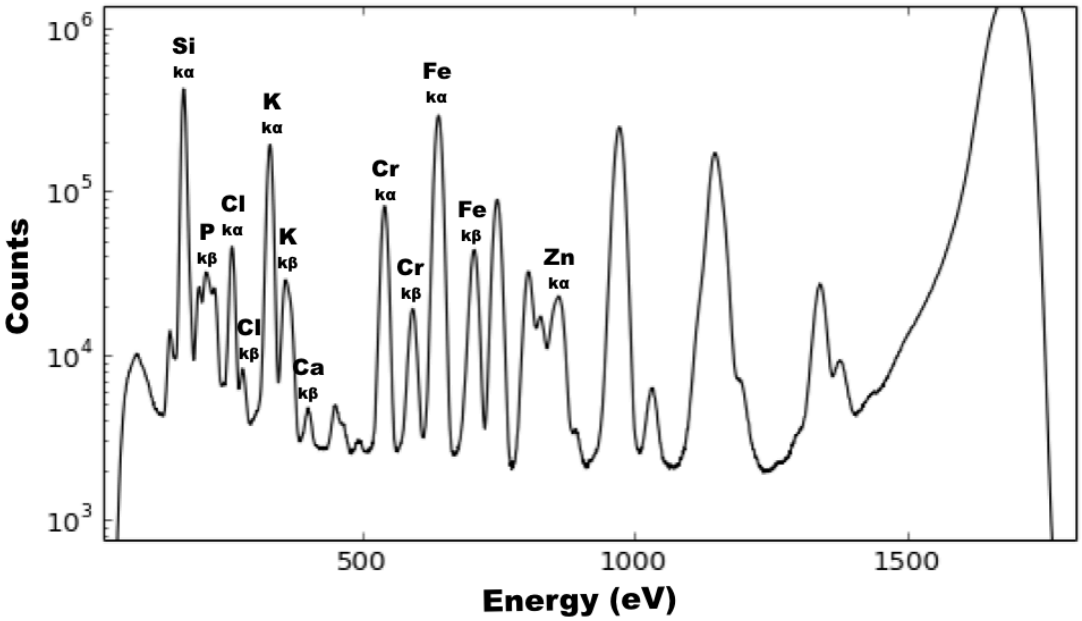

Figure 3.2 - Typical fluorescence spectrum of bMSC. Incident photon energy: 17.05 keV

In order to obtain quantitative data, the acquired spectra were fitted using the PyMCA (*43*) open source software, which was developed at the European Synchrotron Radiation Facility. The program allows interactive as well as batch processing of large data sets and is well suited for X-ray

fluorescence microscopy. The quantification of the fluorescence intensity is based on a fitting procedure of the recorded fluorescence spectra. Spectrum evaluation is made by nonlinear least squares fitting of a mathematical model to the spectral data in order to deal with background and resolve peak overlaps:

$$\chi^2 = \frac{1}{n-m}\sum_i \frac{[y_i - y_{fit}(i)]^2}{y_i} \qquad (3.3)$$

Where:

y is the content of channel i,

$yfit$ is the calculated value of fitting function in this channel,

n is the number of channels

m is the number of parameters in the fitting function.

As the background in XRF spectrum is the result of many processes, its evaluation is not straightforward. However, there are some established strategies how to deal with it. It can be estimated before and thus subtracted from the data before fitting. After this procedure, the area under each peak is obtained, giving the number of counts for that specific fluorescence line. A map giving the spatial distribution of the fluorescence intensity can be obtained.

For a region containing stem cells at 10 days of osteogenic differentiation, a tomographic fluorescence scan was acquired with a pixel size of 125 nm,

in order to access the elemental distribution in three dimensions. 2D maps of cells positioned on the rotation axis were recorded at 28 angles. After fitting with PyMCA and alignment using in-house Octave code, the maps were used for tomographic reconstruction through TomoJ (*44*), a plugin of ImageJ (*45*). An iterative method using Total Variation regularization was selected for tomographic reconstruction. This resulted in 3D maps of Ca, P, and Zn distributions. The output of the reconstruction is a stack of virtual slices or tomograms, which for better visualization has been converted to 3D renderings, obtained after manual segmentation using Chimera (*46*) open source software.

From the Ca and Zn fluorescent maps of the BMSC @4^{th} and 10^{th} day of differentiation, it was possible to calculate Zn/Ca values. To obtain these ratios, the moles of Ca and Zn of the analyzed mineral nuclei were calculated, multiplying the respective XRF maps (expressed in areal mass (g/cm^3)) for the pixel area and normalizing for respective atomic weight.

3.3 X-ray absorption near-edge spectroscopy (XANES)

X-ray absorption near-edge spectroscopy was performed at the MISTRAL beamline of the ALBA synchrotron (*47*, *48*). Varying the energy of the incident photons on the sample across the Ca L -edge, ER-TXM directly detects Ca and its chemical state, as it provides a full Ca L-edge absorption spectrum at each image pixel, with a spatial resolution of a few tens nm.

On selected areas 2D XANES images (12 s exposure time, effective pixel size 10 nm, field of view (FOV) 13 μm × 13 μm) were collected varying the energy across the Ca L-edge with a variable spectral sampling (0.5 – 0.1 eV). The chosen value for the fixed focus constant of the variable line spacing plane grating monochromator (*48*) was 1.5 in order to optimize the compromise between spectral resolution (≈ 0.2 eV) and the rejection of the grating second harmonic. The objective zone plate lens and the CCD detector positions were automatically adjusted to maintain the sample in focus and constant magnification. The necessary total acquisition time was about 1.5 hours per energy scan, including the flat field acquisition at each energy step.

XANES measurements were performed on two bMSC at 10 days and on two bMSC at 4 days. For each cell, five fields of view were selected in such a way to almost cover the full area of the cell. As a consequence, it results that five energy scan were acquired for each cell for a total of twenty measurements. The "images pre-treatment" and "pixels selection" operations were performed on all the measurements. The "spectra analysis by peak deconvolution" was performed only on the selected spectra (one from a BMSC at 4 days and one from a BMSC at 10 days). It is worth noting that the BMSC at 4 days samples showed a bigger spectral variety respect with the BMSC at 10 days. Each image of the energy stack (I (x,y), where I is the transmitted intensity by the sample and x and y are the 2D coordinates of a generic pixel) is firstly normalized to unity dividing by the corresponding Flat Filed image (I_0 (x,y), being I_0 the incident intensity on the sample), taking into account the value of the electron current in the

storage ring, and then aligned taking as reference the first image. The alignment is done by a homemade software (SW) selecting a suitable region of interest (ROI). The ROI of a single image is compared with the ROI of the first image and thanks to the Python library of cv2 (Open Computer Vision: OpenCV) the SW uses the normalized cross-correlation of both ROIs to detect the best matching between them (the function used is 'cv2.matchTemplate ()'). Once this best matching is detected, the number of pixels calculated in the precedent operation shifts the image. This process is repeated for each image of the energy stack. Normally this operation reduces the effective field of view of about 10%-15%, i.e. from 13 μm × 13 μm to ≈ 11 μm × 11 μm. At this point, a full Ca L-edge X-ray Absorption Spectrum (XAS) at each image pixel can be extracted. In particular, the absorbance for each pixel (A) as a function of the energy can be calculated from the measured intensities using the *Beer-Lambert law*:

$$A = t\mu = -\ln\left(\frac{I}{I_0}\right) \tag{3.4}$$

Where:

t is the thickness

μ is the linear absorption coefficient of the material.

Spectra were extracted only from pixels in the field of view containing Ca. Pixels containing Ca are those pixels with a Signal (S) to Noise (N) ratio bigger than two, i.e. S/N>2, with S defined as the absorbance difference between the average absorbance value around the L_2 peak maxima (352.3 eV – 352.7 eV) and the absorbance average value in the pre-edge energy

region (344 eV–346.5 eV) and N defined as the sigma in the pre-edge energy region. Pixels selection operation was performed using ImageJ and TXMWizard softwares (*49*, *50*).

Peaks deconvolution was performed in order to compare the measured spectra. In a first step a linear background correction is performed interpolating the data points in the 344 eV – 346.5 eV (pre-edge energy region) with a straight line and subtracting it to the total spectra, in order to eliminate the contribution of lower energy absorption. This operation is done using a homemade routine implemented in Matlab. In particular, the fit is performed using the Matlab function "polyfit", i.e. the calculated straight line is the best linear fit of the data points in the pre-edge energy region in a least-squares sense. Then the edge steps at the Ca L_2, L_3 -edges resulting from transitions to the continuum were also subtracted using a double arctan function, as described in (*49*, *50*).

$$\frac{h_1}{\pi}\left\{atan\left[\frac{\pi}{w_1}(E-E_1)\right]+\frac{\pi}{2}\right\}+\frac{h_2}{\pi}\left\{atan\left[\frac{\pi}{w_2}(E-E_2)\right]+\frac{\pi}{2}\right\}+C \quad (2.5)$$

With:

$w_1 = w_2 = 0.2$ eV,

E_1 = L2 $peak_{max}$

E_2= L2 $peak_{max}$ + 3 eV.

The others parameters h_1, h_2, C , were fitted with the data points in the pre-edge (344 eV – 346.5 eV) and in the post-edge (355.8 eV -360 eV) energy regions.

These two operations (linear background subtraction and double arctan subtraction), applied to the Ca $L_{2,3}$-edges spectrum of the HA reference sample, are illustrated in Figure 3.3.

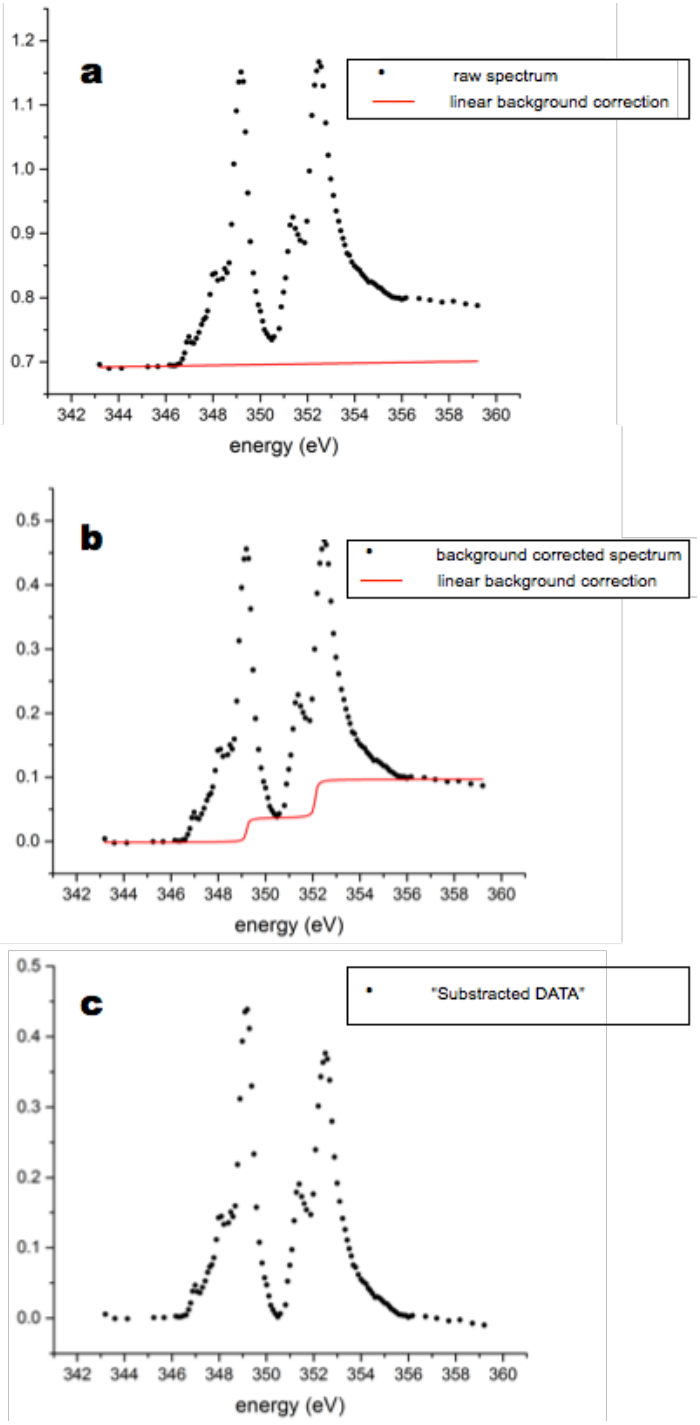

Figure 3.3 – a) Linear background and b) double arctan subtraction showed for the HA reference sample. c) The "subtracted DATA" are the experimental points on which the Gaussians fit was performed.

Following Beniash et al. (*51*), the data after this double subtraction ("subtracted data") are fitted with 7 or 5 Gaussians (the chosen number of Gaussians corresponds to the best fit) using the tool "Peak Analyzer" of Origin® software. Fitting results are reported in Figure 3.4.

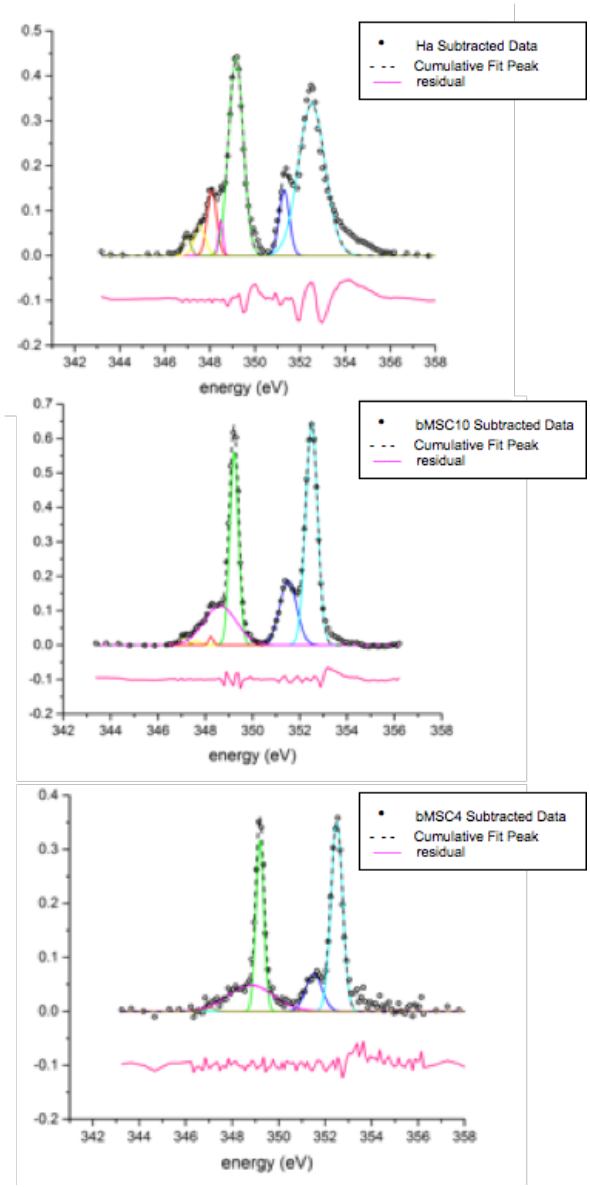

Figure 3.4 - Ca L edge Gaussian fits for the subtracted data reported in the main text (HA, bMSC10 and BMSC4). The subtracted data (empty circles) are over imposed with the Gaussians used for the fits and the cumulative fit which is simply the sum of the Gaussian curves (dashed lines). The corresponding residual, calculated as the difference between the subtracted data and the cumulative fit is also reported, vertically shifted for sake of clarity.

Details on the peaks fit parameters are reported in Table 3.1.

BMSC4		Value	Standard Error
Peak1(Gaussian)	xc	347.0634	0.27232
Peak1(Gaussian)	A	0.00316	0.00603
Peak1(Gaussian)	w	0.43784	0.73408
Peak2(Gaussian)	xc	348.7958	0.12042
Peak2(Gaussian)	A	0.11839	0.01162
Peak2(Gaussian)	w	2.29355	0.32177
Peak3(Gaussian)	xc	349.1931	0.00559
Peak3(Gaussian)	A	0.13657	0.00652
Peak3(Gaussian)	w	0.40554	0.01597
Peak4(Gaussian)	xc	351.5148	0.04513
Peak4(Gaussian)	A	0.06064	0.00744
Peak4(Gaussian)	w	0.82879	0.12052
Peak5(Gaussian)	xc	352.50000	0.00761
Peak5(Gaussian)	A	0.21872	0.00631
Peak5(Gaussian)	w	0.58772	0.01786
BMSC10		**Value**	**Standard Error**
Peak1(Gaussian)	xc	347.11244	0.08695
Peak1(Gaussian)	A	0.00878	0.00536
Peak1(Gaussian)	w	0.36765	0.20343
Peak2(Gaussian)	xc	347.62067	0.16938
Peak2(Gaussian)	A	0.00496	0.01337
Peak2(Gaussian)	w	0.36962	0.62407
Peak3(Gaussian)	xc	348.24092	0.05063
Peak3(Gaussian)	A	0.00582	0.00649
Peak3(Gaussian)	w	0.22356	0.1852
Peak4(Gaussian)	xc	348.63695	0.1271
Peak4(Gaussian)	A	0.19441	0.02098
Peak4(Gaussian)	w	1.60671	0.16664
Peak5(Gaussian)	xc	349.22691	0.00322
Peak5(Gaussian)	A	0.26227	0.00907
Peak5(Gaussian)	w	0.4387	0.00999
Peak6(Gaussian)	xc	351.50833	0.0146
Peak6(Gaussian)	A	0.16815	0.00633
Peak6(Gaussian)	w	0.84361	0.03829
Peak7(Gaussian)	xc	352.50000	0.00366
Peak7(Gaussian)	A	0.4059	0.00551
Peak7(Gaussian)	w	0.59534	0.0085
HA		**Value**	**Standard Error**
Peak1(Gaussian)	xc	346.96418	0.23915
Peak1(Gaussian)	A	0.01871	0.02901
Peak1(Gaussian)	w	0.41351	0.37816
Peak2(Gaussian)	xc	347.55357	0.47415
Peak2(Gaussian)	A	0.03911	0.11437
Peak2(Gaussian)	w	0.56412	1.28968
Peak3(Gaussian)	xc	348.08607	0.17356
Peak3(Gaussian)	A	0.07534	0.1132
Peak3(Gaussian)	w	0.48911	0.48683
Peak4(Gaussian)	xc	348.47364	0.05218
Peak4(Gaussian)	A	0.01881	0.02459
Peak4(Gaussian)	w	0.22477	0.13979
Peak5(Gaussian)	xc	349.15099	0.01168
Peak5(Gaussian)	A	0.35646	0.01179
Peak5(Gaussian)	w	0.76594	0.03117
Peak6(Gaussian)	xc	351.29468	0.02867
Peak6(Gaussian)	A	0.0826	0.01256
Peak6(Gaussian)	w	0.533	0.07166
Peak7(Gaussian)	xc	352.50000	0.02346
Peak7(Gaussian)	A	0.49785	0.01759
Peak7(Gaussian)	w	1.38511	0.059

Table 3.1 - Fitting results. The used formula for the Gaussian function is:

$$y = \left(A/w\sqrt{PI/4 \cdot \ln(2)}\right) e^{\left(-4\ln(2)\times\left({(x-xc)2}/{w^2}\right)\right)} \qquad (3.6)$$

Fits were shifted to have the L_2 peak centered at 352.5 eV

3.4 X-ray diffraction techniques: Small/Wide Angle X-ray Scattering

Small (SAXS) and Wide Angle X-ray Scattering (WAXS) techniques were used to study supra- and sub-molecular structural ordering of the investigated samples. In SAXS sample electron-density inhomogeneity is monitored at a nanometric scale, in WAXS at atomic scale. The SAXS/WAXS scanning microscope, of the X-ray MicroImaging Laboratory (XMI-L@b)) @IC-BARI is equipped with a Rigaku Fr-E+ SuperBright rotating anode table-top microsource (Cu Kα, λ=0.15405 nm, 2475W), a multilayer focusing optics (Confocal Max-Flux; CMF 15-105) and a three-pinhole camera (SMAX-3000). An image plate (IP) detector with 100 μm pixel size and a 6mm hole at the center was placed at about 3 cm from the sample to acquire WAXS data, while collecting the SAXS data. The SAXS detector is a Triton 20 gas-filled photon counter with ~ 200 μm pixel size, which was placed at about 2.2 m from the sample. Once acquired 2D data were calibrated by means of the standard reference materials (Si NIST SRM 640b for WAXS and silver behenate for SAXS data) and folded into 1D profiles. A detailed description of the XMI-L@b performances can be found in Altamura et al. and Sibillano et al (*52*, *53*) The raw SAXS data, collected in scanning mode, were composed into a microscopy, as explained in (*54*).

Scanning SAXS 2D data were recorded, spatially resolved, across a 0.9 x 0.9 mm^2 area (Figure 3.5, top left) with the WAXS detector simultaneously

collecting the 2D data (Figure 3.5, top right), averaged in the same area. A schematic layout of the set-up is showed in the bottom of Figure 3.5.

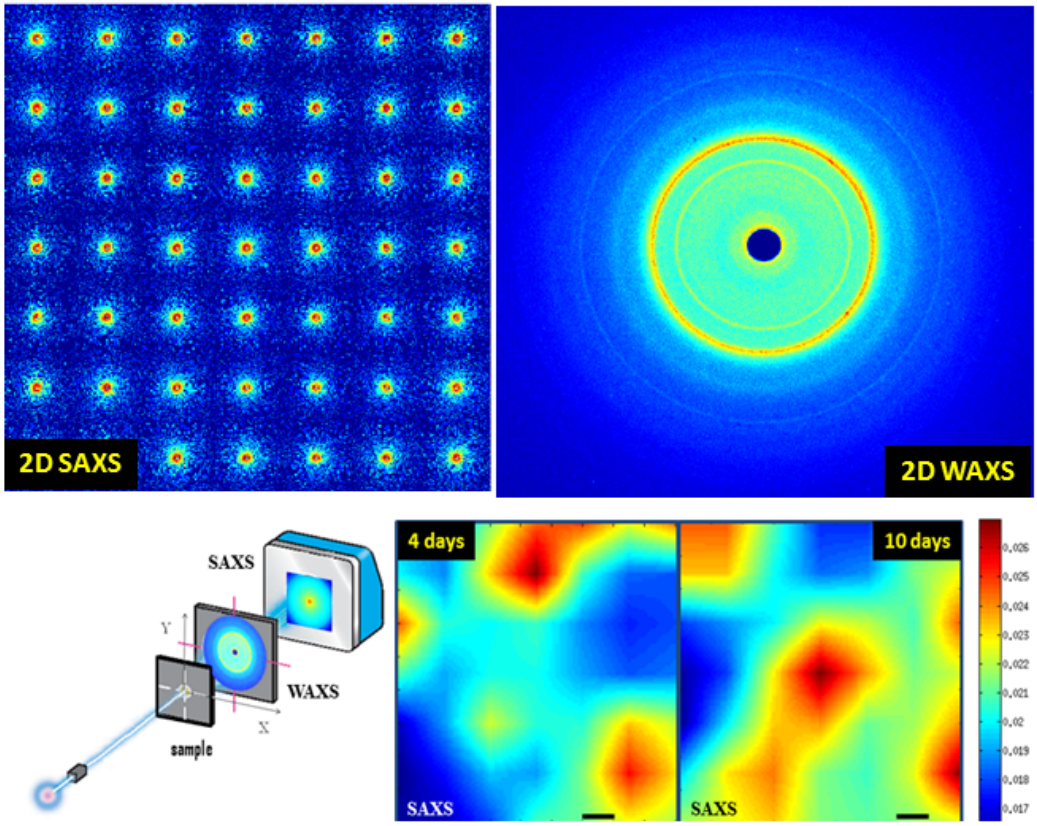

Figure 3.5 - Scanning SAXS 2D data recorded across a 0.9x0.9 mm^2 area (top left); 2D WAXS (top right), averaged in the same area; schematic layout of the set-up (bottom left); SAXS scanning microscopies of samples 4days (bottom center) and 10 days (bottom right). Scale bar = 0.1 mm.

SAXS and WAXS raw 2D data were centered, calibrated and folded (*54*) into 1D profiles. The SAXS 1D profiles were then integrated in the measured scattering range, and the integrated intensity was normalized to the transmitted intensity and plotted as an image in Figure 3.5 for samples at 4^{th} day (bottom center) and 10^{th} day (bottom right) of differentiation. The red/blue colored regions indicate area with the highest/lowest scattering.

The WAXS 1D profiles where first qualitatively analyzed with the QUALX program (*55*) to identify the structure which can explain the measured diffraction peaks. This qualitative analysis was followed by a quantitative whole profile fitting analysis of the diffraction profiles, performed using the FULLPROF program (*50*), based on the Rietveld approach. Two samples at 10^{th} day of osteogenic induction (bMSC_10days_A and bMSC_10days) and one sample at 4^{th} day of differentiation (bMSC_4days_4C) were analyzed with the same procedure.

The volume (V) of the unit cell was calculated from the lattice constant lengths and angles.

For the general unit cell (*56*):

$$V = abc\sqrt{1 + 2\,cos\alpha\,cos\beta\,cos\gamma - cos^2\alpha - cos^2\beta - cos^2\gamma} \qquad (3.7)$$

With $\alpha = 90°$, $\beta = 90°$:

$$V = abc\sin\gamma \qquad (3.8)$$

3.5 Samples preparation for Synchrotron-based techniques

For Synchrotron-based techniques at the beam line ID16A-NI 'Nano-Imaging, bMSC were grown on silicon nitride membranes Si_3N_4 considered as ideal support for XRF analysis (from Silson Ltd., Northampton (UK), 5x5 mm^2 size, 4 mm^2 membrane area, 200 *nm* membrane thickness and 200 μm frame thickness).

The cells were plated at a concentration of 1×10^4 cell/cm^2 on membrane windows previously sterilized in ethanol, under previously described culture conditions (considered as ideal). After 4 and 10 days from the osteogenic induction, the attachment and spreading of the cells were carefully verified using optical microscopy. Cell culture medium was removed and the membranes were briefly washed in 100 nM freshly prepared ammonium acetate solution for two times, to remove salts and trace metals from the medium. The cells were frozen-hydrated by a rapid plunge freezing in liquid ethane bath cooled with liquid nitrogen (Figure 3.6). As vitreous ice upon the samples causes X-ray absorption, excess water is removed before plunge freezing via blotting.

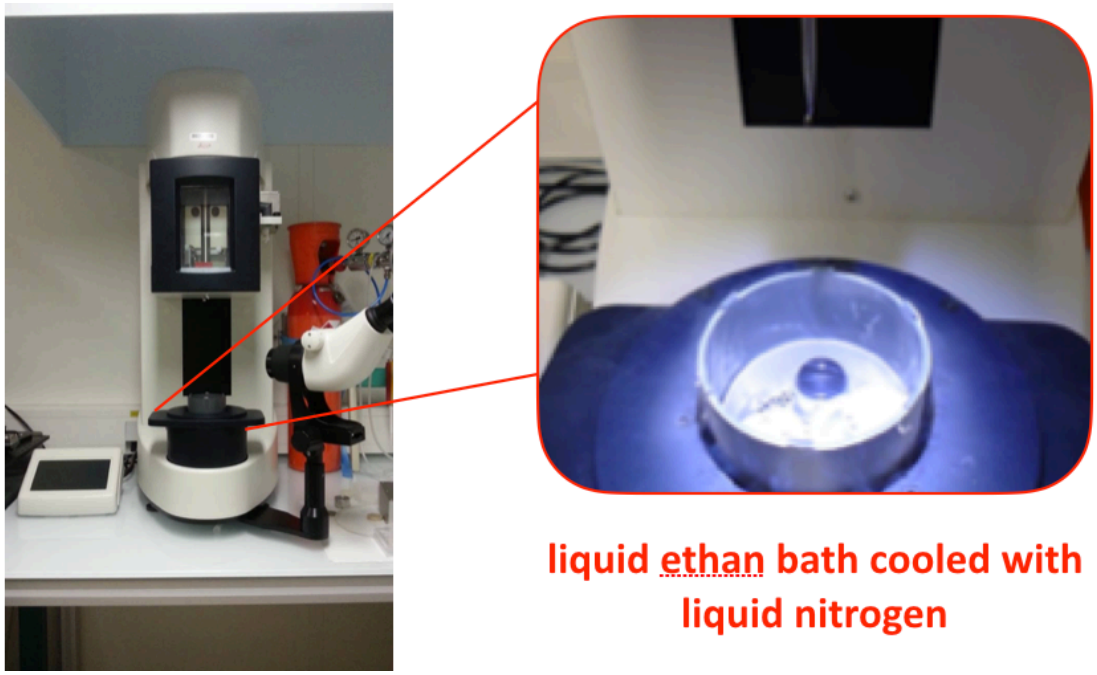

Figure 3.6 - Automatic plunge freezing system

After plunge freezing, a cryogenic workflow is maintained until and during the XRF measurements. Wafers are transferred into the liquid nitrogen bath of a Leica™ EM VCM (Vacuum Cryo Manipulation System), where they are clamped in a pre-cooled gold-coated VCT sample holder. The sample holder can then be loaded into the Leica™ EM VCT500 (Vacuum Cryo Transfer system) (Figure 3.7).

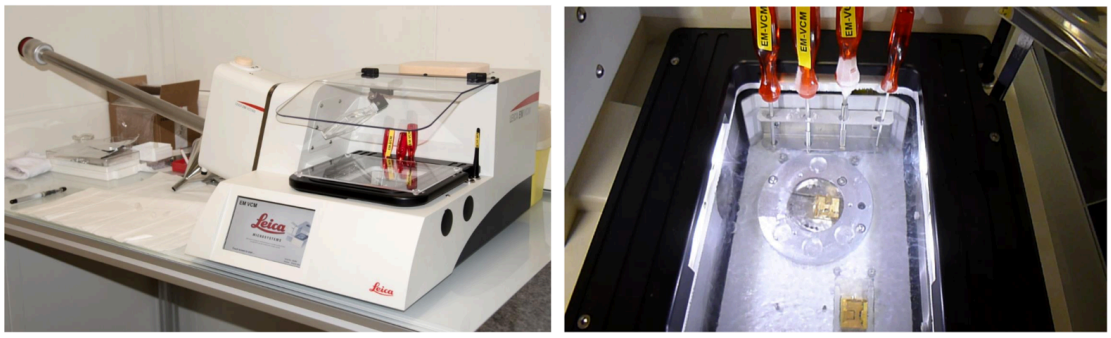

Figure 3.7 - a) Cryo loading chamber and transfer system. b) Transfer shuffle

Finally, sample shuttle is attached to the ID16A-NI vacuum chamber and the gold-coated copper cube holding the silicon nitride membrane with deposited cells is transferred onto the sample stage kept at -150°*C*. An external visible light microscope system with long working distance positioned outside the vacuum chamber is used to bring bMSC in the focus of the X-ray nanobeam.

For the acquisition at MISTRAL beamline of the ALBA synchrotron, cells were seeded onto gold quantifoil R 2/2 holey carbon-film microscopy grids and after 4 or 10 days vitrified by plunge freezing (as described previously). The frozen grids were then transferred into the Mistral transmission x-ray microscope under cryogenic conditions. Artificial hydroxyapatite (HA) reference sample was prepared finely crushing HA powder (Sigma–Aldrich) in a mortar, and lying down the obtained micrometer and sub-micrometer dust on a Quantifoil® Au TEM grid.

3.6 Samples preparation for diffraction techniques

The cells were plated at a concentration of 1×10^4 cell/cm^2 on silicon membrane windows (from Silson Ltd., Northampton (UK), 5x5 mm^2 size, 4 mm^2 membrane area, 200 *nm* membrane thickness and 200 μm frame thickness), previously sterilized in ethanol. After 4 and 10 days from the osteogenic induction, cell culture medium was removed and the membranes were washed briefly in 100 mM ammonium acetate for two times, then fixed in methanol / acetone 1:1 at the temperature of -20° C for 5 minutes. Then the solution of methanol-acetone was removed and the cells on silicon membranes were dried at room temperature.

4. Results and Discussion

4.1 Osteogenic differentiation and Gene Expression Evaluation

bMSC were stimulated to differentiate toward osteoblasts using an osteogenic cocktail (Chapter 2.2) for 4 and 10 days. In order to assess mineralization of extracellular matrix, the samples were stained and analyzed by optical microscope. To this aim, a standard Alizarin Red staining was used to quantify the calcium/calcium salts deposition occurred during the extracellular mineralization.

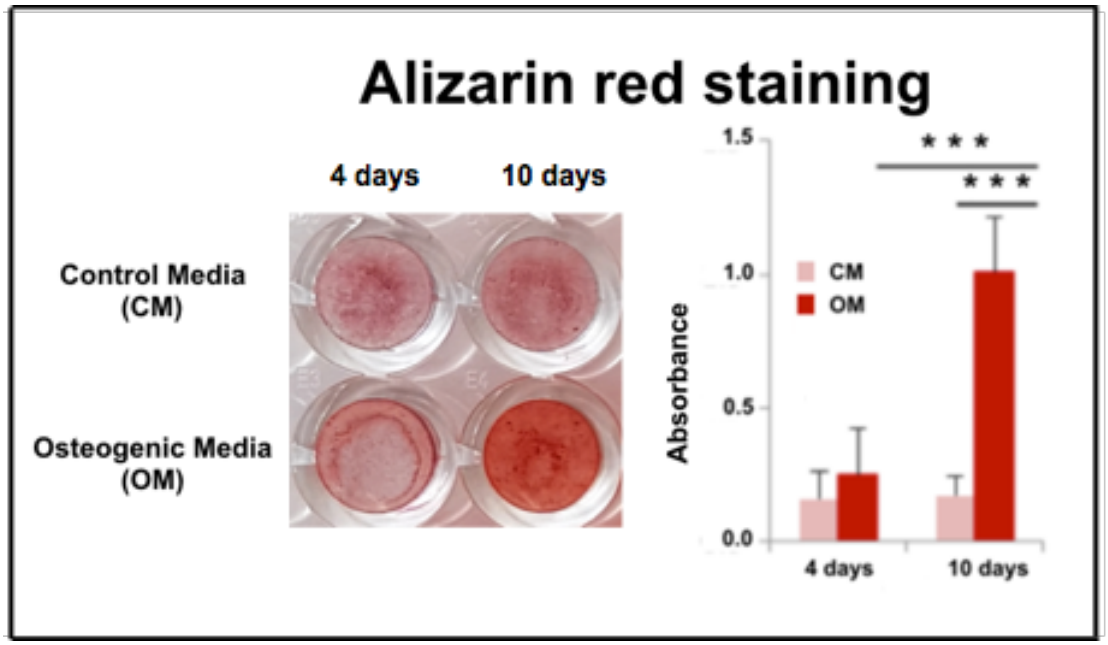

Figure 4.1 - Alizarin Red staining was performed after exposure to osteogenic medium for 4 and 10 days. Photographs of a representative plate were taken (left). After acid extraction the absorbance was measured at 562 nm (right). The results shown are the mean ± standard deviation of four experiments in triplicate. Statistical significance was determined using Student's t test. *** $P<0.001$.

Photographs of a representative plate (Figure 4.1 left panel) showed that, after 4 days of stimuli, no calcium deposits in the extracellular matrix are detectable, unlike the bMSC @10^{th} day of stimuli. In fact, the medium of the plate exposed for ten days to the osteogenic medium (OM) took on a red colour compared to the medium of the plate exposed for 10 days to the control medium (CM). This suggests the detection of calcium nodules in the extracellular matrix, by the Alizarin red staining. On the contrary, there is no difference in the colour between the medium of the plate exposed for 4 days to the osteogenic and control medium, suggesting no detection of calcium nodules in the extracellular matrix.

The absorbance was measured at 562 nm (Figure 4.1 right panel) following acid extraction. No significance difference was detected between the BMSC exposed to the OM for 4 days and the BMSC exposed to CM. On the contrary, there is a significance difference between BMSC exposed to OM for 10 days and the BMSC exposed to CM.

By real time-PCR, the expression of characteristic osteogenic genes is evaluated.

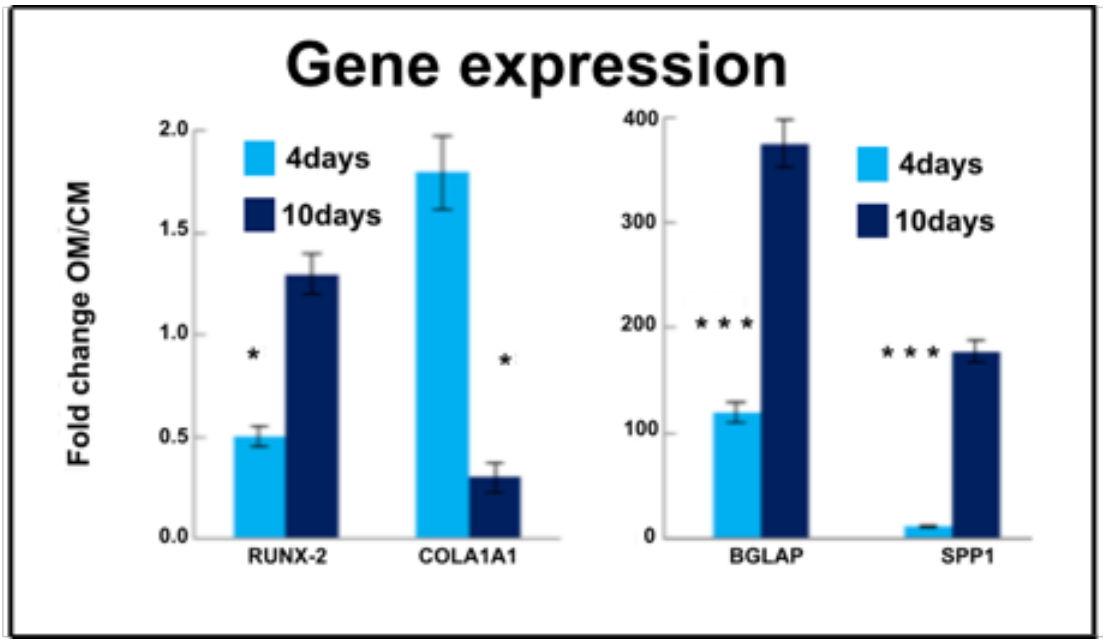

Figure 4.2 - Real-Time PCR was performed three times in triplicate on RNA extracted from BMSC using primers designed on RUNX2, COL1A1, BGLAP and SPP1 sequence. The results are shown as the mean ± standard deviation. Statistical significance was determined using Student's t test. *** P<0.001.

In agreement with Cazzaniga et al. (*32*) and Sargenti et al. (*31*), a significant increase of the transcript for RUNX2, the master regulator of osteogenesis, was detected in bMSC @10th day of stimuli (Figure 4.2). In addition to RUNX2, we also evaluated COL1A1, an early marker of osteoprogenitor cells, and SPP1 and BGLAP, coding for non-collagenous proteins, associated with a more mature differentiation.

COL1A1 was maximally expressed @4th day; in fact, it is related to the early stages of osteogenic process. BGLAP was already significantly up-

regulated @4th day, whereas SPP1, a potent protein nucleator of hydroxyapatite, was maximally expressed @10th day.

The over-expression of these osteogenic genes confirms the differentiation of the bMSC.

4.2 Electron density and chemical composition of mineral nuclei

4.2.1 2D phase contrast imaging

The synchrotron-based phase contrast imaging was performed to investigate on the electron density of the mineral nuclei of the bMSCs @4th and 10th day of osteogenic induction. After retrieving the phase as described in Chapter 2.4.1, considering the four images, each at its own magnification, the final results are the phase maps. The Figure 4.3 shows the phase contrast maps of the sample @ 4th day of differentiation.

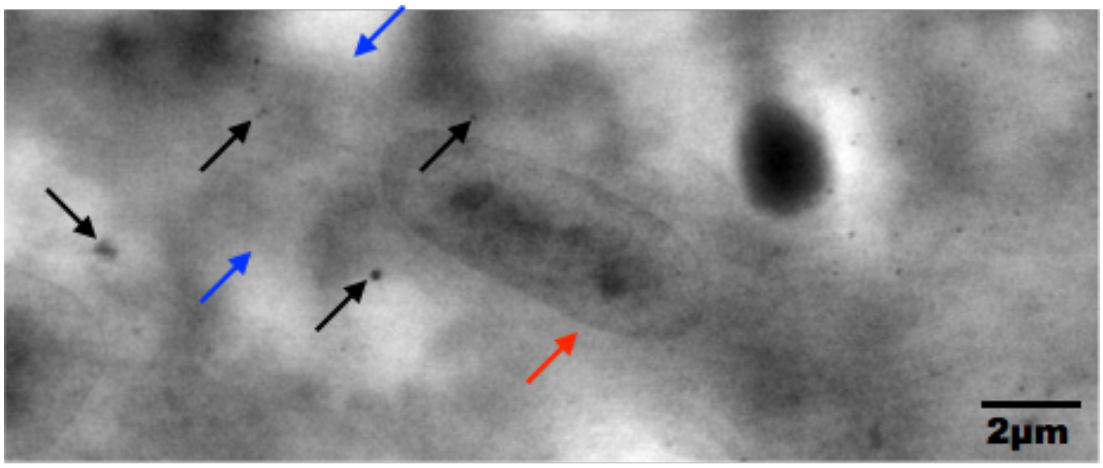

Figure 3.3 - Phase contrast reconstructed map of a sample after 4 days of differentiation (pixel size 100 nm). The red arrow indicates the nucleus of the cell. The blue arrows indicate the cytoplasm and the black arrows highlighted the intracellular mineral nuclei.

There are few small depositions, as highlighted by the black arrows. The red and blue arrows indicate respectively the nucleus and the cytoplasm of the cell. From this 2D map, it seems that the mineral nuclei are intracellular.

As regards the samples @10th day of differentiation, we acquired the phase contrast data of the same sample at high resolution, 15 and 7 nm.

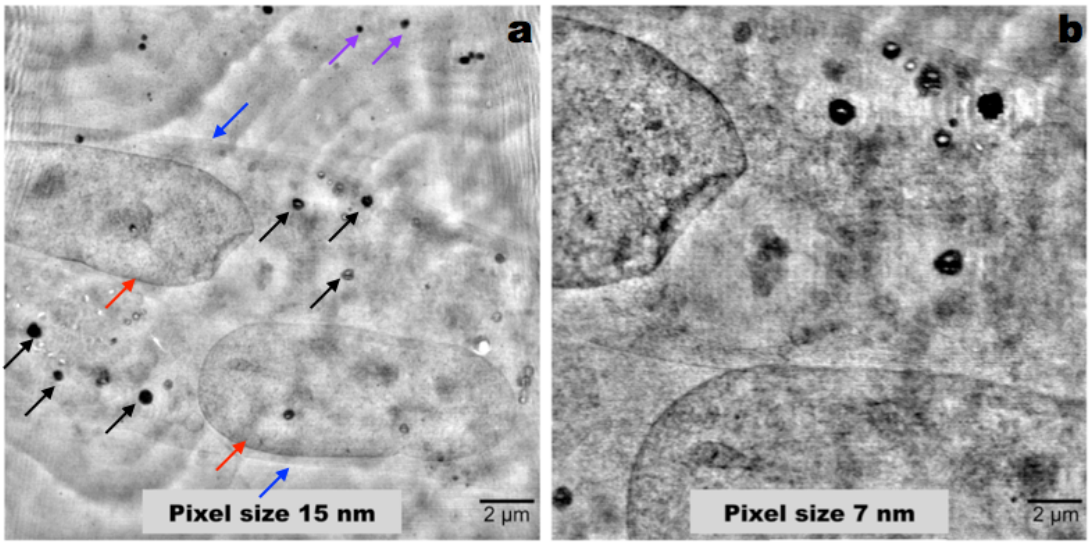

Figure 4.4 - Phase contrast reconstructed maps of a sample after 10 days of differentiation (pixel size: a) 15 nm, b) 7 nm). In the panel a, the red arrows indicate the nuclei of two cell. The blue arrows indicate the cytoplasm of the two cells; the black arrows highlighted the intracellular mineral nuclei, while the violet ones indicate the extracellular mineral granules.

At this time of differentiation, there are a lot of mineral nuclei. The red and blue arrows indicated respectively the nuclei and cytoplasm of two cells. Some of depositions are clearly outside the cells (violet arrows in Figure 4.4 left panel), while others are mainly near inner part of the plasma membrane (black arrows in Figure 4.4 left panel). The 2D phase contrast maps limit the investigation to two dimensions since the results are averaged over the sample thickness (projections). There is no certainty that the depositions, seems to be intracellular, are really inside the cell and eventually in which area of the cell they are localized.

4.2.2 X-ray phase contrast nano-tomography

The inability to derive the elemental distribution over the sample thickness could lead to a misinterpretation of phase contrast maps (*21*). Therefore, we acquired X-ray phase contrast nano-tomography on bMSC. We obtained the 3D localization of the mineral nuclei across the entire cell thickness both at 4 and 10 days of differentiation. As explained in Chapter 2.4.1, the output of the holographic nano-tomography reconstruction is set of 2000 tomograms. The output is a "zeta-stack", i.e. an analysis of the cell by sections along the zeta axis, which provides the three-dimensional distribution of the sample.

After this first reconstruction, unfortunately, the projections are affected by missing wedge artefacts. In Figure 4.5, it is possible to observe the first reconstruction of the sample @10^{th} day of differentiation, before and after the correction of the missing wedge. Replacing with zeros the projections affected by missing wedge artefacts, we obtained a better reconstruction of the tomography (Figure 4.5 b).

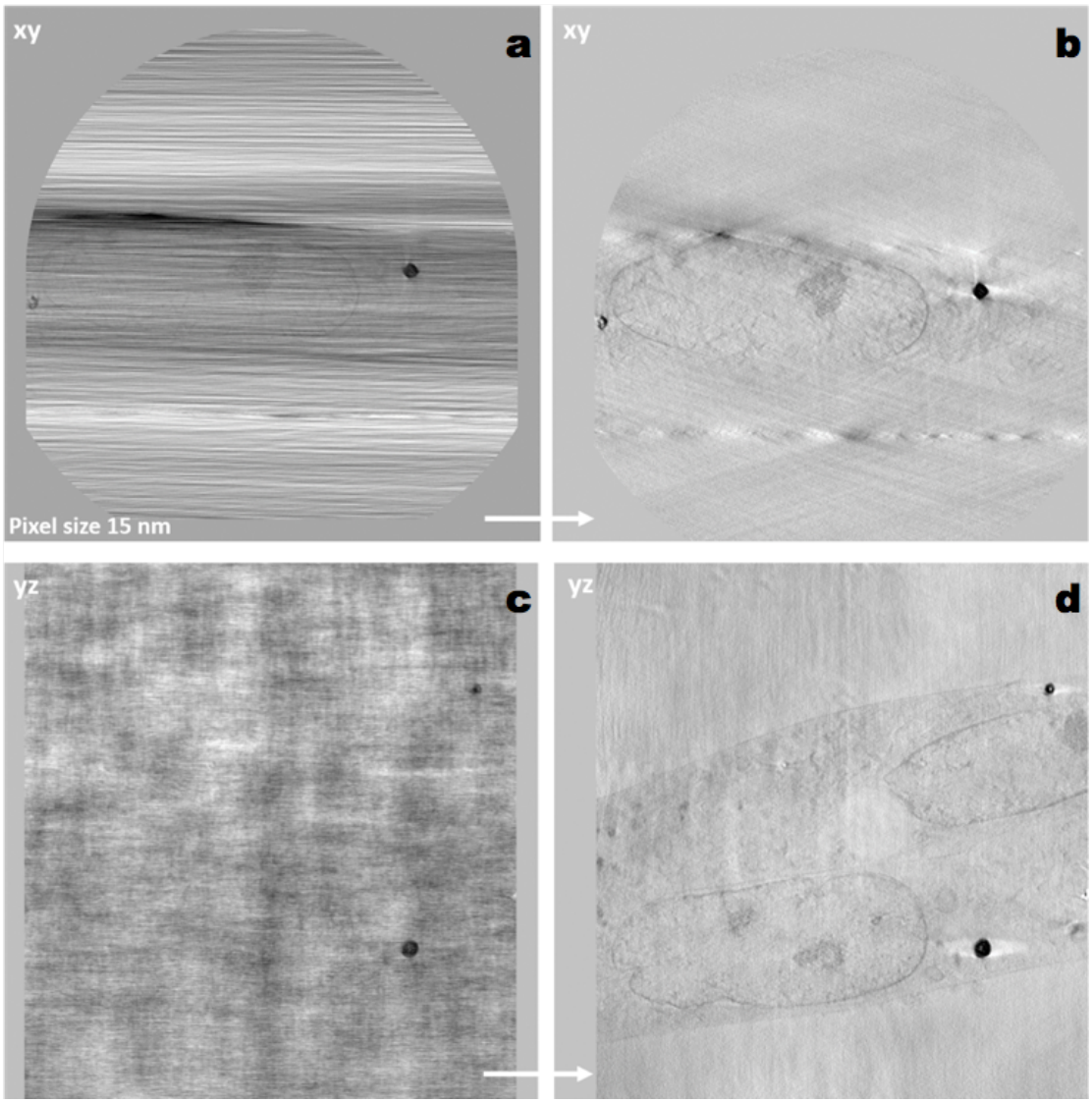

Figure 4.5 – a - c) nano-tomography projection affected by missing wedge artefacts (respectively xy and yz view); b - d) same nano-tomography projection (respectively xy and yz view) after the correction of the artefacts.

After this correction, 3D renderings were realized through a manual segmentation in Chimera software. Specifically, for each projection of the z-stack, the two nuclei, the respective cytoplasm and the mineral

depositions were segmented (Figure 4.6).

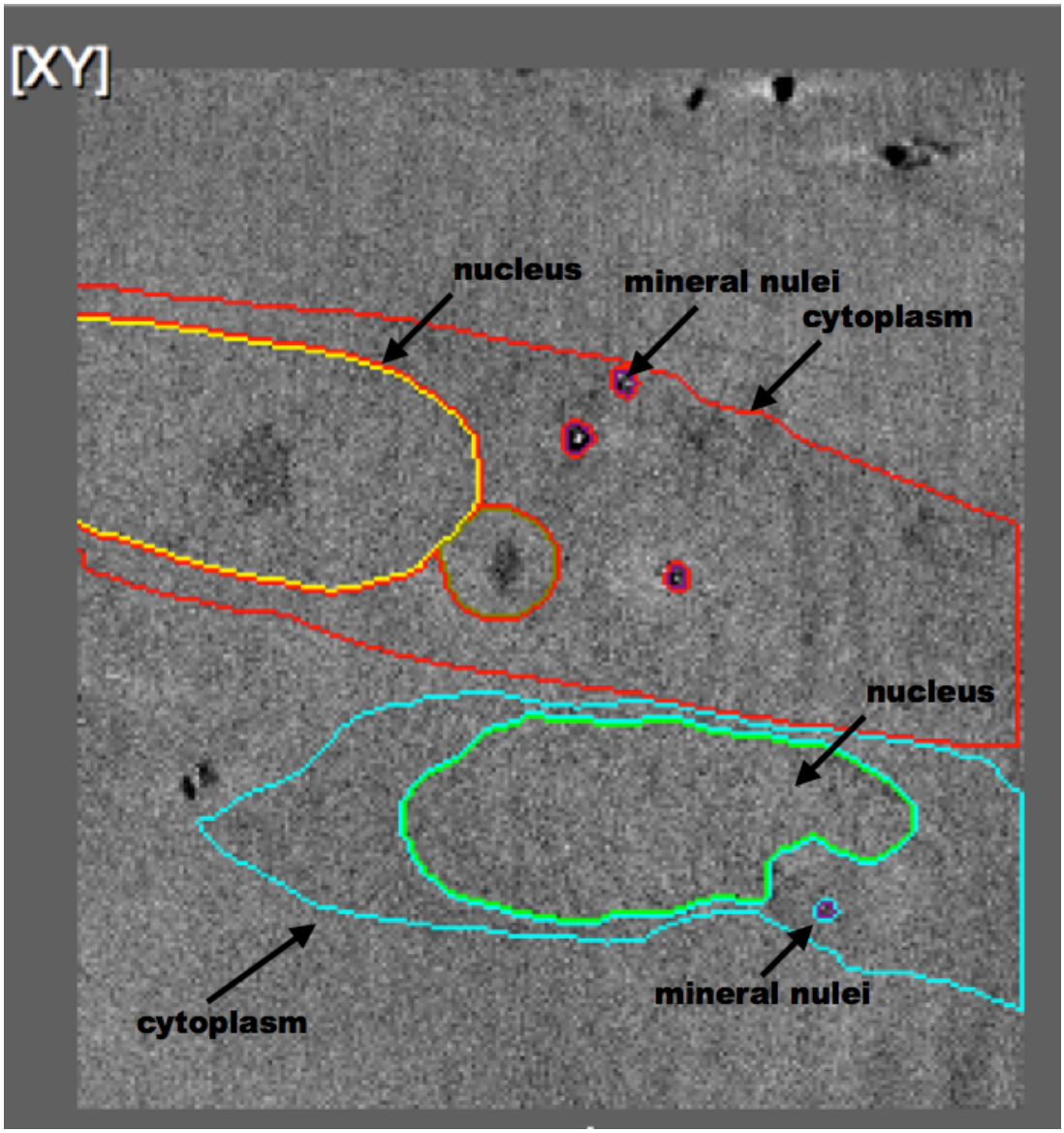

Figure 4.6 – Projection of the z-stack in which nuclei, cytoplasm and the mineral depositions were segmented.

Then, we performed the 3D nano-rendering of the intracellular structure and mineral nuclei deposition (Figure 4.7) to better visualize the 3D information given by the reconstructed electron density.

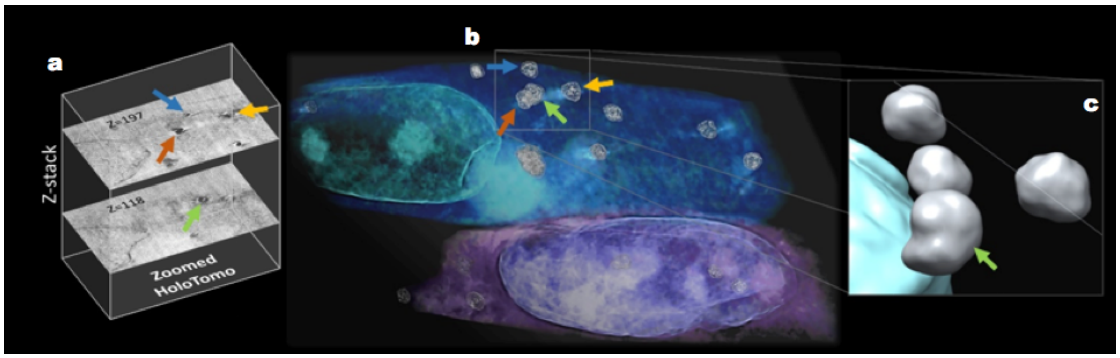

Figure 4.7 – a) two slices of the z-stack reconstructed from the phase-contrast tomography, b) volume rendering of the phase contrast nano-tomography data; the colored arrows indicate four intracellular depositions, c) zoomed 3D solid nano-rendering of the four granules highlighted in b).

Figure 4.7 a shows two slices of the z-stack reconstructed from the phase-contrast nano-tomography. In Figure 4.7 b, it is possible to observe the 2D image of the volume nano-rendering of the sample: the colored arrows indicate four intracellular depositions. For these four mineral granules, we performed a zoomed 3D solid nano-rendering (Figure 4.7 c).

Several mineral nuclei are localized in the cytoplasm of the cell (Figure 4.7), confirming that the first steps of the biomineralization take place intracellular. This is in agreement with a study on a mouse cell model of bone formation employing nano-analytical electron microscopy techniques, which identified intracellular Ca accumulation (*57*). The 3D phase contrast

imaging allows us to reconstruct both the three-dimensional intracellular sub-organelles and mineral nuclei (Figure 4.7).

4.2.3 2D X-ray fluorescence microscopy

The only way to obtain the elemental distribution maps at nanoscale in single cell is the use of synchrotron-based techniques (*21*).

In this PhD project, synchrotron-based X-ray fluorescence microscopy (XRFM) was exploited to determine the chemical composition of mineral nuclei at the nanometric scale in the early stages of the biomineralization. Non-induced bMSCs and samples after 4 and 10 days of osteogenic differentiation were analyzed.

Specifically, we evaluated the hydroxyapatite constitutive elements, Ca and P and the main HA substitutive ion, Zn.

The spatial resolution and sensitivity of synchrotron X-ray fluorescence microscopy enabled precise chemical characterization of the mineral nuclei despite their small dimensions, with volumes ranging between 0.01 and 2.5 μm^3.

As regards the non-induced cells, no mineral nuclei were detected in the Ca, P and Zn maps (Figure 4.8 A, B and C).

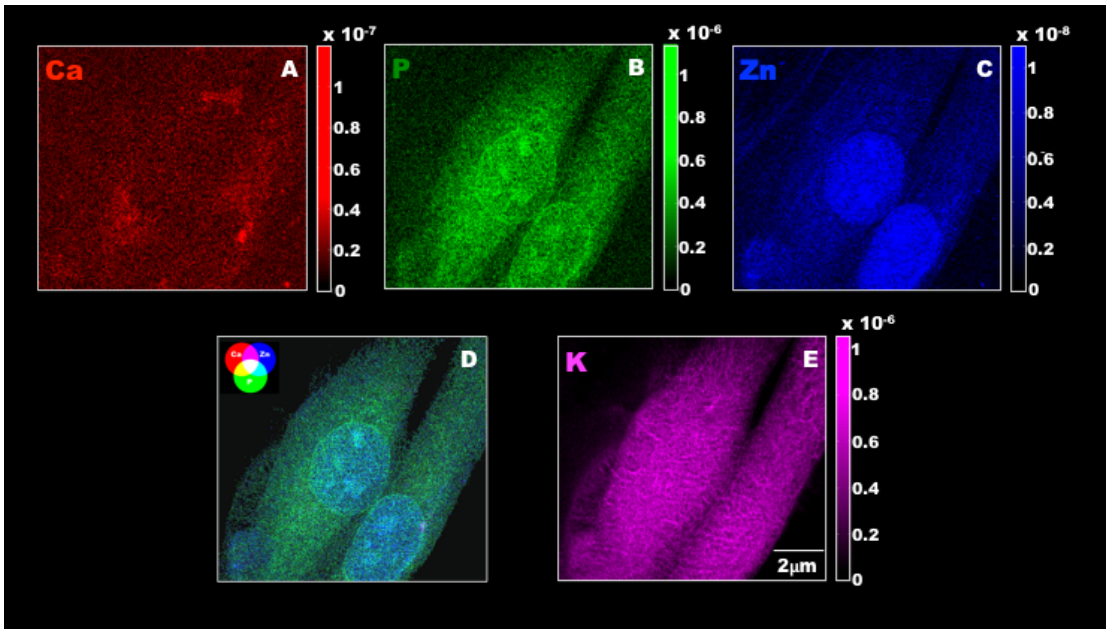

Figure 4.8 - The elemental distribution maps express in g/cm^2 (pixel size 70 nm)) of Ca (red) P (green), Zn (blue) and K (magenta) of non-induced bMSCs. The composite map has been generated merging the map of Ca, P and Zn.

We analyzed also the Potassium K line (Figure 4.8 E). Potassium is an essential component of the cells, that is found to be homogeneously distributed throughout the cell, and can therefore give cell conformation.

To verify the co-localization of the three elements (Ca, P and Zn), a composite map was generated through the merging of red, green and blue colours (Figure 4.8 D).

On the other hand, the fluorescence maps of the samples @4th day of osteogenic induction (Figure 4.8 first column) some mineral nuclei are present, as indicated by coloured arrows in fluorescence maps.

These data indicated that biomineralization starts early just after 4 days of the osteogenic induction.

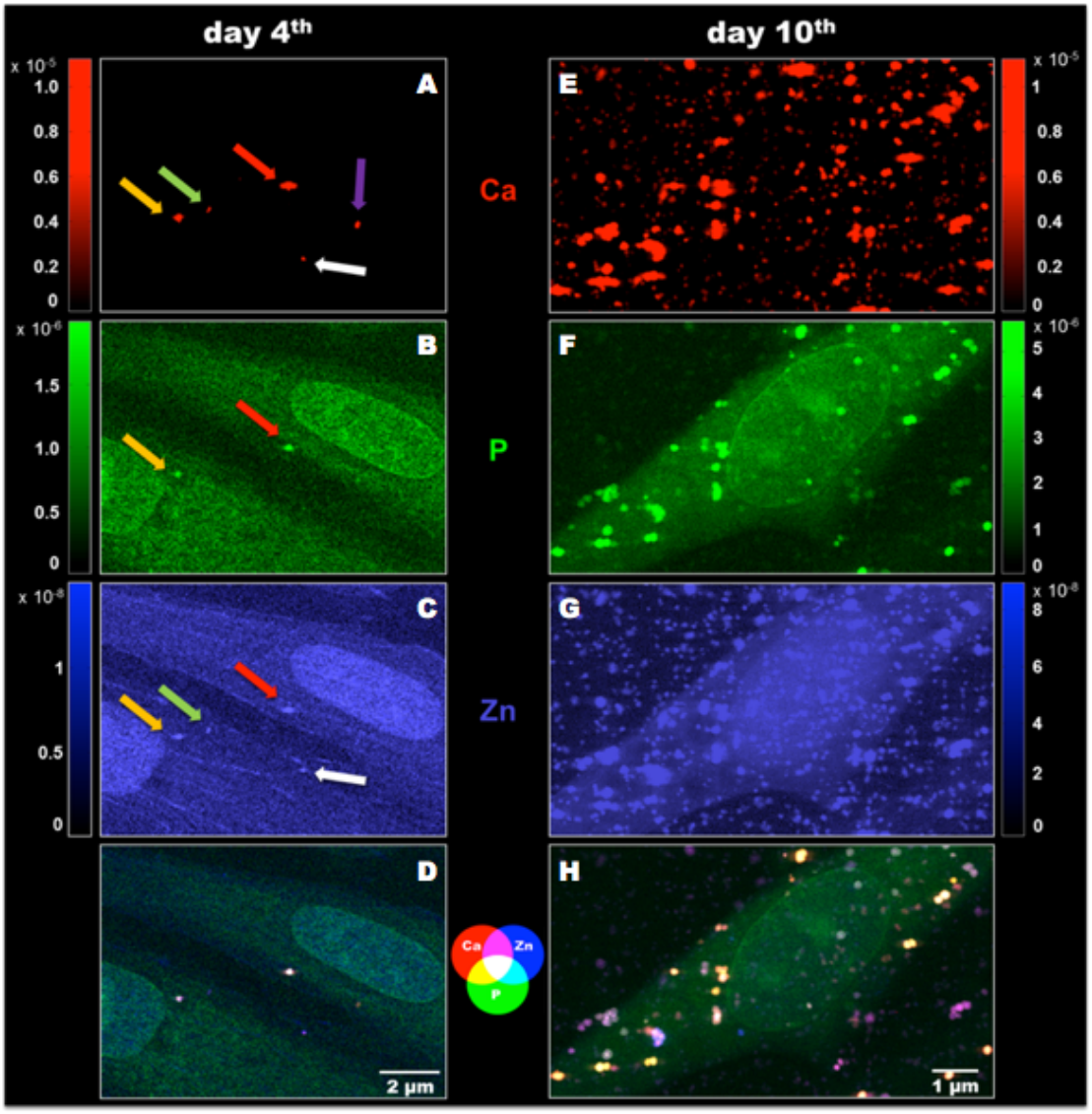

Figure 4.9 - 2D X-ray fluorescence maps (pixel size 70 nm, expressed in areal mass (g/cm^2)) showing the evolution between day 4 and day 10 of bMSC osteogenic differentiation. (A, E) Red: elemental maps of Ca. (B, F) Green: elemental maps of P. (C, G) Blue: elemental maps of Zn. (D, H) Composite elemental distribution of Ca, P and Zn.

Focusing on the Ca map (Figure 4.9 A), it can be noted that the mineral nuclei, indicated by the red and yellow arrows are also visible in the P and Zn maps (Figure 4.9 B C). Therefore, in these two granules, there is the co-localization of the three elements, as confirmed by the composite map (Figure 4.9 D). In fact, in this map, the two mineral nuclei assume a white colour, highlighting the merging of the three colours then the co-presence of the three elements.

Continuing to observe the Ca map (Figure 4.9 A), the white and red arrows indicate two depositions that are only present in the Zn map (Figure 4.9 C), while the granule indicated by the violet arrow is not present in the P map, nor in the Zn map (Figure 4.9 C).

These results suggested a different timing of elemental accumulation in the five detected mineral nuclei (coloured arrows Figure 4.9 A). The process of Ca deposition can start as a compound, which is not bound to phosphate. A plausible alternative anion candidate is carbonate, since its content in the bone mineral is known to be about 4–8 wt.% (*58*). It is feasible that initial mineral nuclei formation starts as Ca-carbonate compounds, which subsequently incorporate Zn, thus starting HA nucleation by integrating phosphates to build the final structure of HA (*59*).

An unexpected result, obtained from these fluorescence analyzes, was the occurrence of a germinal Zn presence. It is well known that Zn is an element present in the bone, as a substitution ion in hydroxyapatite. In general, its presence is related to its inhibitory activity to osteoclastic bone resorption. Bandyopadhyay et al. (*60*) demonstrate that Zn increases densification and mechanical properties of HA. Bigi et al. (*61*) study the

role of Zn on crystal growth and thermal stability of HA and they showed that the presence of Zn in solution inhibits the crystallization of hydroxyapatite. In this project, it is demonstrated the presence of the Zn at so few days of osteogenic differentiation, so it promotes the new bone formation, confirming what was said by Webstar et al. (*62*).

This represents a novel finding providing an experimental evidence of what was long time ago hypothesized about the role of Zn in HA nucleation (*19*, *57*, *63–65*).

Another consideration that can be made looking these fluorescent maps is that it was possible to detect intracellular mineral deposits after just 4 days of differentiation, while the results obtained with "alizarin red staining" (Chapter 4.1) showed that no calcium depositions were detected in the extracellular matrix at this time of differentiation. Indeed, synchrotron-based techniques have many advantages, which make it much more powerful than traditional laboratory-based source.

After 10 days of osteogenic differentiation, the mineral nuclei are massive in terms of both dimension and number (Figure 4.9 E, F, G).

The elemental analysis revealed different degrees of Ca, P and Zn co-localization as displayed in the composite map shown in Figure 4.9 H. The elements co-localize quite heterogeneously, as shown by the different colours of mineral nuclei in the composite map (Figure 4.9 H).

In order to better investigate the heterogeneity of these mineral depositions @10^{th} day of osteogenic induction, we acquired fluorescent element maps of single mineral nuclei, at high resolution (15 nm pixel size).

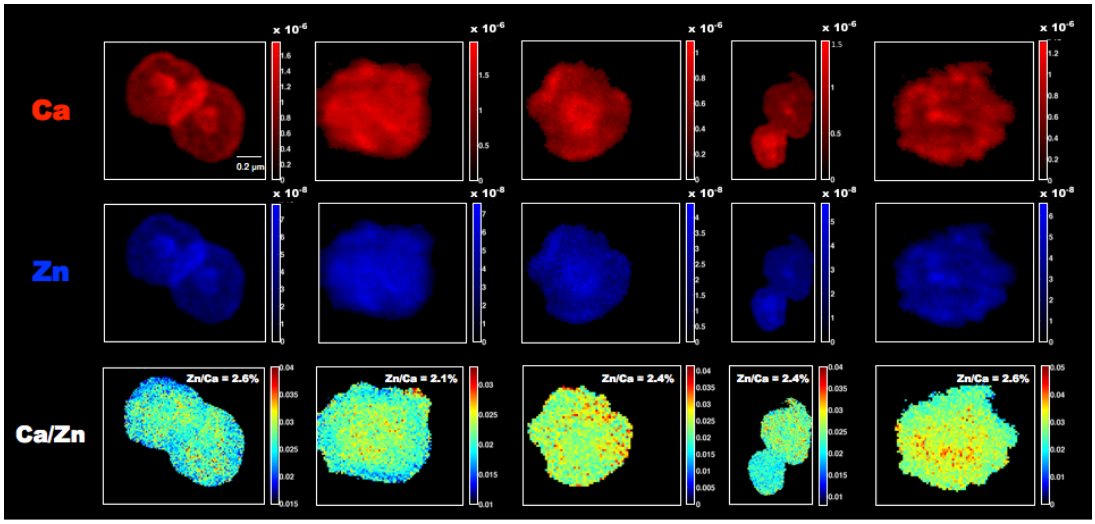

Figure 4.10 – X-ray fluorescence microscopy measurements acquired at 15 nm pixel size (expressed in areal mass (g/cm^2)) in single mineral nuclei formation reporting the Ca, Zn composition and Zn/Ca ratio.

The Zn/Ca ratios of mineral nuclei at 4^{th} and 10^{th} days of differentiation were calculated, as described in Chapter 2.4.2.

It is interesting to note that at 10 days the Zn/Ca ratio in mineral nuclei is about 2% (Figure 4.10), which is the value that approximates the Zn/Ca ratio in mature human bone (*63*).

The Zn/Ca values were also calculated for the mineral nuclei @4^{th} day of stimuli. The Table 4.1 shows the ratio of both differentiated samples, revealing an increase of the Zn/Ca values in bMSC @10th day of differentiation. This increase of Zn quantity in mineral nuclei seems to supports the interpretation that the process of Zn-Ca substitution is taking

place between 4 and 10 days from the beginning of osteogenic differentiation.

	(Zn/Ca)%	
MN formations	4 days	10 days
1	0.8%	2.1%
2	0.5%	0.4%
3	0.6%	2.9%
4	0.7%	2.9%
5	0.9%	2.8%
6	0.5%	2.9%
7		2.6%
8		2.4%
9		2.0%
10		2.4%

Table 4.1 - Zn/Ca ratio in bMSC exposed to the differentiation cocktail at 10 *versus* 4 days.

4.2.4 X-ray Fluorescence Tomography

The three-dimensional phase contrast described in the Chapter 2.4.1 has allowed having information about the electron density and spatial location of the depositions inside the cells. However, it has not permit to identify the

individual contribution of Ca, P, and Zn to the formation of these intracellular depositions. For this reason, the same cells were scanned by X-ray fluorescence tomography to allow the 3D visualization of elemental distribution (Figure 4.11).

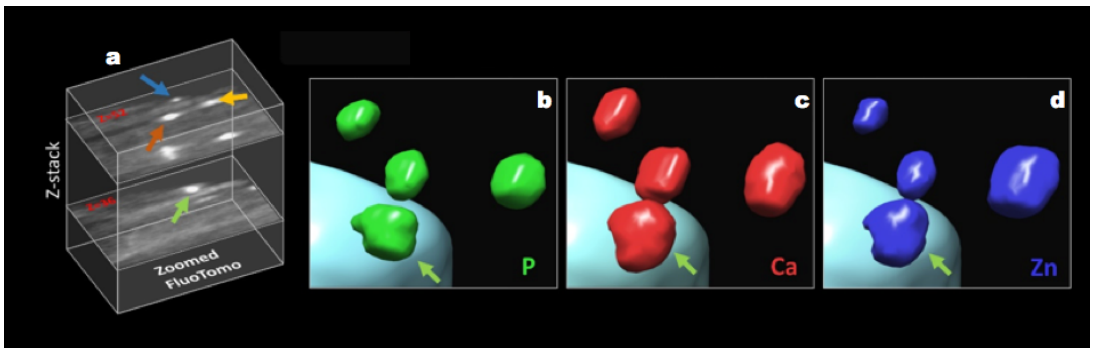

Figure 4.11 - a) two slices of the z-stack reconstructed from the X-ray Fluorescence Tomography; b-c-d) zoomed 3D nano-rendering of P, Ca and Zn intracellular deposition respectively.

In Figure 4.11 b-c-d, it is reported respectively the P, Ca and Zn 3D composition of the same four mineral nuclei highlighted in Figure 4.9 b. Focusing on the mineral deposition indicated by the green arrow, it is possible to observe that Ca gives the major contribution to this granule, followed by Zn and P. This result confirms a different timing of elemental accumulation in the mineral nuclei. As discussed in paragraph 4.2.3, at the beginning of the deposition, it is possible that the mineral nuclei are Ca-carbonate and then they incorporate Zn and phosphates to build the final structure of HA (*59*).

4.3 Crystalline structure of mineral nuclei analyzed by X-ray spectroscopy and diffraction

Since biomineralization culminates with crystalline HA depositions, we employed X-ray spectroscopy and diffraction techniques to gain information at atomic scale on the molecular and crystalline structure of the mineral nuclei.

4.3.1 X-ray absorption near edge structure (XANES) spectro-microscopy

XANES spectro-microscopy was performed on bMSC after 4 and 10 days of osteogenic differentiation to explore the molecular structure of the mineral nuclei.

This technique provides structural information, complementing the other techniques used in this study. Variations in energy positions and in relative intensities of the peaks in the XANES spectra depend on the Ca chemical state (*51*).

A typical Ca $L_{2,3}$ - edges spectrum of calcium compounds presents two main peaks (L_2 and L_3 in Figure 4.12) and a "multi-peak pattern" of relatively lower intensity (peaks a, b, c, d and e in Figure 4.12).

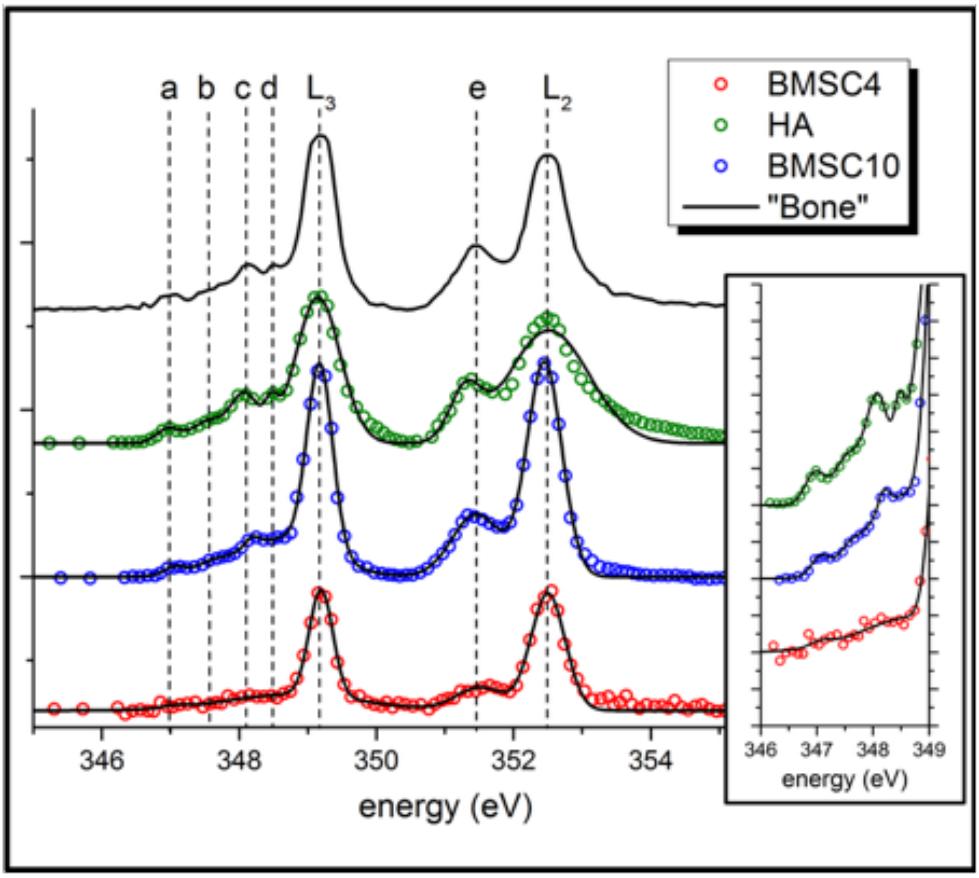

	a	b	c	d	L_3	e	L_2
HA	346.9	347.6	348.2	348.5	349.1	351.3	352.5
BMSC10	347.1	347.6	348.6	348.5	349.2	351.5	352.5
BMSC4	347.1	——	348.8	——	349.2	351.5	352.5

Figure 4.12 - XANES spectra obtained from mineral nuclei localized in bMSC at 4 days (red spectrum), 10 days (blue spectrum), HA reference sample (green spectrum). Best fits (black lines) are superimposed on the corresponding experimental points. A "Bone" spectrum is also reported for further comparison. The inset figure highlights the region of the smaller crystal field peaks a-d. Peaks positions are reported in the table (expressed in eV). Spectral sampling in the peaks region was 0.1 eV, estimated energy resolution is about 0.2 eV.

The “multi-peak pattern” distinguishes the crystalline phases from the amorphous ones both in calcium carbonates and in calcium phosphates compounds. In fact, these low intensity peaks correspond to transition towards crystalline states which do not exist in the amorphous case (*51*, *66–70*). An example of spectra obtained from mineral nuclei in bMSC (red spectrum, bMSC4 at 4 days; blue spectrum, bMSC10 at 10 days) and from HA reference sample (green spectrum, HA) is reported in Figure 4.12. A human bone standard spectrum is also reported as reference. The energy distance of the main L2 peak (352.5 eV) and L3 peak (349.2 eV) are the same for the four spectra. Variations exist in the visibility and relative positions of the “multi-peak pattern” (a, b, c, d in Figure 4.12).

The corresponding observed trend is quite clear: a significant increment in the visibility of the HA crystal field peaks a, b, c, d is revealed moving from the spectrum of the BMSC at 4 days to the one at 10 days and finally to the HA (or the “bone” spectra).

De Groot et al. (1990) (*67*) and Naftel et al. (2001) (*71*) show that the “multi-peak pattern” of the Ca-$L_{2,3}$ edge is the result of the crystal field, whose magnitude and symmetry arise from the arrangement of atoms, so that in amorphous Ca carbonates as well as in amorphous Ca phosphates (ACP), the minor crystal field peaks distinguish the amorphous phases from the crystalline ones (*68*). Beniash et al. demonstrate that for ACP the visibility of these peaks raises increasing the crystallinity and the energy position of peaks appear at lower energy in crystalline than in amorphous phases (*51*).

In this project, the significant increment in the visibility of the HA crystal field peaks is revealed in the mineral nuclei spectra obtained at 10 days *versus* 4 days of differentiation stimuli, suggesting a dynamic process culminating in the formation of mature crystals.

4.3.2 Small and Wide-angle X-ray scattering

The X-ray diffraction techniques, small/wide-angle X-ray scattering (SAXS/WAXS), provide quantitative information of the electron density distribution at nanometric (SAXS) and atomic (WAXS) scales. In particular, SAXS techniques, detailed in the Chapter 2.4, were used to inspect the lateral inhomogeneity of the samples. WAXS data were quantitatively analyzed to explore the crystalline nature (type of atoms, their positions and symmetry) of the compounds.

In crystallography, crystal structure describes the ordered arrangement of atoms, ions or molecules in a crystalline material. This crystal structure occurs from the intrinsic nature of the constituent particles to form symmetric patterns that repeat identical along the principal directions of three-dimensional space in matter. The smallest group of particles in the material that constitutes the repeating pattern is the unit cell of the structure that defines the symmetry and structure of the entire crystal lattice, which is built up by repetitive translation of the unit cell along its principal axes.

The lengths of the principal axes, or edges, of the unit cell and the angles between them are the lattice constants, also called lattice parameters [3].

Indeed, each material produces a unique X-ray diffraction pattern (intensity *versus* scattering angle), which is a fingerprint of its crystalline atomic structure.

The WAXS 1D profiles are shown in Figure 4.13 for samples @4th day (left) and 10th day (right) of osteogenic induction.

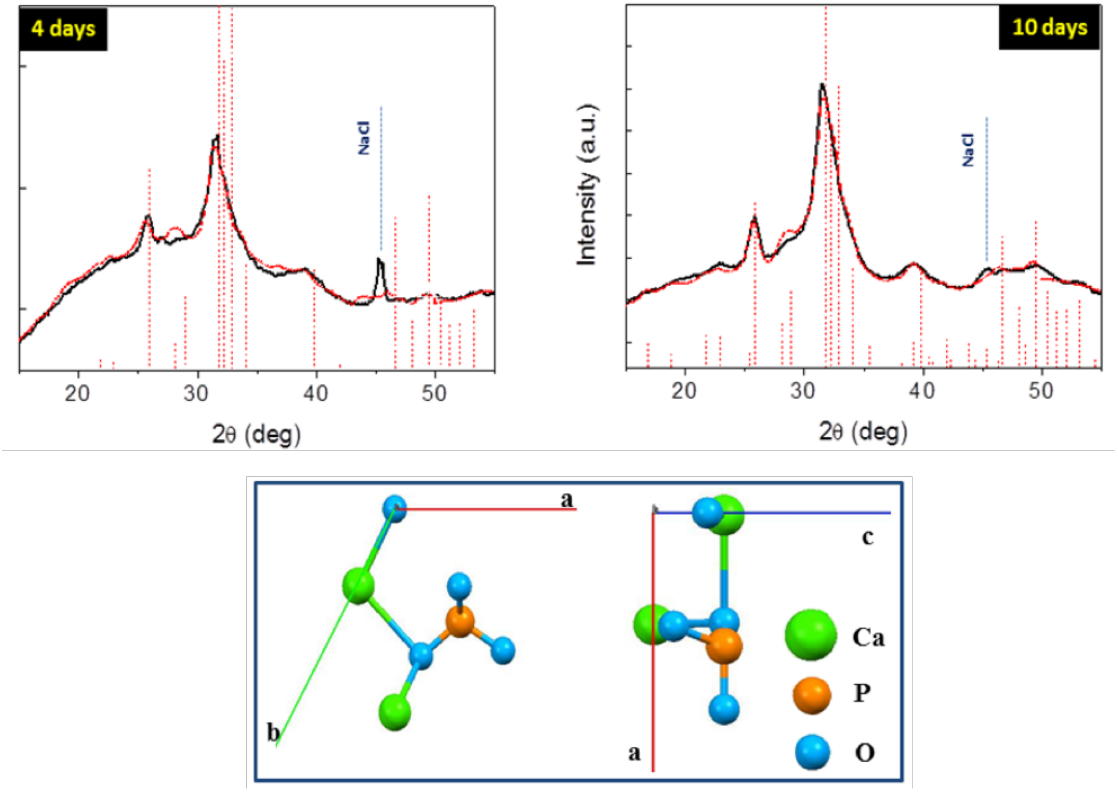

Figure 4.13 - WAXS spectra for samples at 4 days (top left) and at 10 days (top right) identify the hexagonal hydroxyapatite (red profile). The best fits (red profiles) are over-imposed to the experimental data (black profiles). In the second row, projections of the atomic positions within the crystallographic unit cell of the hydroxyapatite structure are shown: along c-axis (left) and along the b-axis (right).

The quantitative analysis of the WAXS spectra (Figure 4.13) allowed identifying the hexagonal HA (red profile) as the unique crystalline structure present in differentiating bMSC. The blue vertical bar corresponds to NaCl taken as internal reference is in the same angular position for both samples.

The best fits (red profiles), obtained for both samples, are over imposed to the experimental data (black profiles). Fits allowed determining that the samples differ for the actual unit cell parameters and cell volume, and for the domain size along the main crystallographic directions ([110] and [002]), as summarized in Table 4.2. We can observe a decrease of the refined cell volume at 10 days respect to 4 days.

	a (*Å*)	**b** (*Å*)	**c** (*Å*)	**α** (°)	**β** (°)	**γ** (°)	**V**	**X**	**App size (nm)**
10days	9.481	9.481	6.906	90	90	120	**537.6**	**0.026**	[002] 4.52±0.99 [110] 4.19±0.99
4days	9.578	9.578	6.949	90	90	120	**552.2**	**0**	[002] 4.45±0.48 [110] 4.52±0.48

Table 4.2 - Unit cell parameters, cell volume and apparent size, after Rietveld analysis

The decrease (2%) of the refined cell volume with the increase of the incubation days can be ascribed to the substitution of Ca with Zn atoms in the HA crystal lattice. In order to quantitatively estimate the percentage of substitution Zn/Ca atoms in the lattice, we relied on the empirical Vegards's rule, which linearly relates the crystal lattice constants of an

alloy to the concentrations of the constituent elements (*72*). Therefore, the value of contraction X in Table 4.2 directly gives the ratio of Zn/Ca.

The Zn substitution causes a volume contraction of the unit cell due to the smallest ionic radii of Zn (1.22 Å) with respect to Ca (1.76Å) (*73*) which means a smaller distance between atoms and therefore a contraction of the crystallographic unit cell volume. Indeed, Zn is a structural part of the HA crystal of human bone and it has been reported that its effect in HA nucleation could cause a gain in the critical size of the HA lattice in the initial phase of mineralization (*63*).

The 2% volume decrease of the hexagonal HA unit cell, and its explanation in terms of substitution of Ca with Zn atoms in the HA crystal lattice, confirmed the XRFM measurements acquired at high resolution (15 nm pixel size) in single mineral nuclei (Table 4.1 and Figure 4.10).

5. Conclusions

The main focus of this work is the study of the early stages of biomineralization by evaluating the genesis of the mineral nuclei depositions and their evolution toward Zn-hydroxyapatite, in human bone mesenchymal stem cells, exposed to an osteogenic cocktail for 4 and 10 days.

Synchrotron-based X-ray techniques provided three-dimensional imaging and chemical element analysis of single cells, enabling to follow the evolution of hydroxyapatite formation in differentiating bMSC during the early phase of the biomineralization process. It is provided a quantitative assessment of the chemical composition of the mineral depositions occurring in the first stage of osteogenic differentiation, together with their molecular and crystal characterization.

In order to drastically mitigate the detrimental effect of the radiation damage and to examine cells as close as possible to their native state, frozen hydrated cells have been analyzed.

The analysis presented in this study revealed that biomineralization starts with hydroxyapatite nucleation within the cell and it rapidly evolves toward a hexagonal hydroxyapatite crystal very similar to the one present in mature human bone, as detected after just ten days of osteogenic induction. Zn inclusion in the mineral depositions favours the nucleation in the hydroxyapatite crystal lattice and at 10 days the process of Zn incorporation is almost complete.

These results were obtained using synchrotron-based techniques that have been pushed to the maximum limit of their potential. In fact, a phase-contrast nano-tomography with a pixel size of 15 nm was acquired and such a high resolution has never been obtained on frozen hydrated cells.

The quantitative phenomenological follow-up of the early stages of biomineralization presented here will serve as a reference for further studies on the intracellular molecular mechanisms governing the initial phase of bone tissue formation.

As future development, aiming to reproduce the bone tissue physiologically conditions, it would be interesting to characterize the initial steps of hydroxyapatite formation in the 3D culture of mesenchymal stem cells, specifically through the use of scaffold templates within a bioreactor system that simulates perfusion and compression.

References

1. R. J. O'Keefe, J. Mao, Bone tissue engineering and regeneration: from discovery to the clinic--an overview. *Tissue Eng. Part B Rev.* **17**, 389–392 (2011).
2. J. P. Gorski, Biomineralization of bone: a fresh view of the roles of non-collagenous proteins. *Front. Biosci. Landmark Ed.* **16**, 2598–2621 (2011).
3. S. Weiner, and H. D. Wagner, THE MATERIAL BONE: Structure-Mechanical Function Relations. *Annu. Rev. Mater. Sci.* **28**, 271–298 (1998).
4. D. J. Prockop, A. Fertala, The Collagen Fibril: The Almost Crystalline Structure. *J. Struct. Biol.* **122**, 111–118 (1998).
5. A. Cedola *et al.*, Engineered bone from bone marrow stromal cells: a structural study by an advanced x-ray microdiffraction technique. *Phys. Med. Biol.* **51**, N109 (2006).
6. W. C. Hartwig, The anatomy and biology of the human skeleton by D. Gentry Steele and Claud A. Bramblett. Texas A & M University Press, College Station, 1988. *Clin. Anat.* **3**, 151–153 (1990).
7. H. Gao, Application of Fracture Mechanics Concepts to Hierarchical Biomechanics of Bone and Bone-like Materials. *Int. J. Fract.* **138**, 101 (2006).
8. B. M. Abdallah, M. Kassem, Human mesenchymal stem cells: from basic biology to clinical applications. *Gene Ther.* **15**, 109–116 (2008).
9. D. J. Prockop, A. Fertala, The Collagen Fibril: The Almost Crystalline Structure. *J. Struct. Biol.* **122**, 111–118 (1998).
10. A. Cedola *et al.*, Engineered bone from bone marrow stromal cells: a structural study by an advanced x-ray microdiffraction technique. *Phys. Med. Biol.* **51**, N109 (2006).
11. F. Betts, N. C. Blumenthal, A. S. Posner, G. L. Becker, A. L. Lehninger, Atomic structure of intracellular amorphous calcium phosphate deposits. *Proc. Natl. Acad. Sci. U. S. A.* **72**, 2088–2090 (1975).
12. F. Nudelman *et al.*, The role of collagen in bone apatite formation in the presence of hydroxyapatite nucleation inhibitors. *Nat. Mater.* **9**, 1004–1009 (2010).
13. S. Scaglione *et al.*, Order versus Disorder: In vivo bone formation within osteoconductive scaffolds. *Sci. Rep.* **2**, 274 (2012).
14. R. A. Young, J. C. Elliott, Atomic-scale bases for several properties of apatites. *Arch. Oral Biol.* **11**, 699–707 (1966).
15. J. F. Kay, Calcium phosphate coatings for dental implants. Current status and future potential. *Dent. Clin. North Am.* **36**, 1–18 (1992).
16. P. Bhattacharjee, H. Begam, A. Chanda, S. K. Nandi, Animal trial on zinc doped hydroxyapatite: A case study. *J. Asian Ceram. Soc.* **2**, 44–51 (2014).
17. H. Kawamura *et al.*, Stimulatory effect of zinc-releasing calcium phosphate implant on bone formation in rabbit femora. *J. Biomed. Mater. Res.* **50**, 184–190 (2000).

18. A. Ito *et al.*, Zinc-releasing calcium phosphate for stimulating bone formation. *Mater. Sci. Eng. C*. **22**, 21–25 (2002).
19. M. Rohde, H. Mayer, Exocytotic process as a novel model for mineralization by osteoblasts in vitro and in vivo determined by electron microscopic analysis. *Calcif. Tissue Int.* **80**, 323–336 (2007).
20. J. C. Riviere, S. Myhra, *Handbook of Surface and Interface Analysis: Methods for Problem-Solving, Second Edition* (CRC Press, 2009).
21. E. Malucelli *et al.*, Where is it and how much? Mapping and quantifying elements in single cells. *The Analyst*. **141**, 5221–5235 (2016).
22. S. Mobilio, F. Boscherini, C. Meneghini, Eds., *Synchrotron Radiation* (Springer Berlin Heidelberg, Berlin, Heidelberg, 2015; http://link.springer.com/10.1007/978-3-642-55315-8).
23. J. M. Cowley, *Diffraction Physics* (Elsevier, 1995).
24. A. Thompson, D. Vaughan, C. for X-ray optics and advanced light source, X-ray Data Booklet (2000).
25. S. . WILKINS, T. Gureyev, D. Gao, A. POGANY, A. Stevenson, Phase-Contrast Imaging Using Polychromatic Hard X-Rays. *Nature*. **384**, 335–338 (1996).
26. E. Kosior *et al.*, Combined use of hard X-ray phase contrast imaging and X-ray fluorescence microscopy for sub-cellular metal quantification. *J. Struct. Biol.* **177**, 239–247 (2012).
27. G. Henderson, D. Neuville, R. Downs, *Spectroscopic Methods in Mineralogy and Material Sciences* (Walter de Gruyter GmbH & Co KG, 2014).
28. A. H. Compton, The Spectrum of Scattered X-Rays. *Phys. Rev.* **22**, 409–413 (1923).
29. O. Glatter, O. Kratky, *Small angle x-ray scattering* (Academic Press, London; New York, 1982).
30. J. R. Hook, H. E. Hall, *Solid state physics* (John Wiley & Sons, Chichester, West Sussex, U.K., 2010; http://public.eblib.com/choice/publicfullrecord.aspx?p=1212553).
31. A. Sargenti *et al.*, Magnesium Deprivation Potentiates Human Mesenchymal Stem Cell Transcriptional Remodeling. *Int. J. Mol. Sci.* **19** (2018), doi:10.3390/ijms19051410.
32. A. Cazzaniga, J. A. M. Maier, S. Castiglioni, Impact of simulated microgravity on human bone stem cells: New hints for space medicine. *Biochem. Biophys. Res. Commun.* **473**, 181–186 (2016).
33. Gerchberg, O. Saxton, A practical algorithm for the determination of the phase from image and diffraction plane pictures. *Optik*. **35**, 237–246 (1972).
34. M. Krenkel, M. Bartels, T. Salditt, Transport of intensity phase reconstruction to solve the twin image problem in holographic x-ray imaging. *Opt. Express*. **21**, 2220–2235 (2013).
35. P. Cloetens, R. Barrett, J. Baruchel, J.-P. Guigay, M. Schlenker, Phase objects in synchrotron radiation hard x-ray imaging. *J. Phys. Appl. Phys.* **29**, 133 (1996).
36. S. Cagno *et al.*, Combined Computed Nanotomography and Nanoscopic X-ray Fluorescence Imaging of Cobalt Nanoparticles in Caenorhabditis elegans. *Anal. Chem.*

89, 11435–11442 (2017).
37. B. De Samber *et al.*, Nanoscopic X-ray fluorescence imaging and quantification of intracellular key-elements in cryofrozen Friedreich's ataxia fibroblasts. *PloS One*. **13**, e0190495 (2018).
38. A. Bartesaghi *et al.*, Classification and 3D averaging with missing wedge correction in biological electron tomography. *J. Struct. Biol.* **162**, 436–450 (2008).
39. L. Kováčik *et al.*, A simple Fourier filter for suppression of the missing wedge ray artefacts in single-axis electron tomographic reconstructions. *J. Struct. Biol.* **186**, 141–152 (2014).
40. S. BOHIC *et al.*, Synchrotron hard x-ray microprobe: Fluorescence imaging of single cells. *Appl. Phys. Lett.* **78**, 3544–3546 (2001).
41. R. Ortega *et al.*, Cobalt distribution in keratinocyte cells indicates nuclear and perinuclear accumulation and interaction with magnesium and zinc homeostasis. *Toxicol. Lett.* **188**, 26–32 (2009).
42. E. Kosior, S. Bohic, H. Suhonen, P. Cloetens, Absolute zinc quantification at the sub-cellular level by combined use of hard X-ray fluorescence and phase contrast imaging techniques. *J. Phys. Conf. Ser.* **463**, 012021 (2013).
43. V. A. Solé, E. Papillon, M. Cotte, P. Walter, J. Susini, A multiplatform code for the analysis of energy-dispersive X-ray fluorescence spectra. *Spectrochim. Acta Part B At. Spectrosc.* **62**, 63–68 (2007).
44. C. MessaoudiI, T. Boudier, C. O. S. Sorzano, S. Marco, TomoJ: tomography software for three-dimensional reconstruction in transmission electron microscopy. *BMC Bioinformatics*. **8**, 288 (2007).
45. C. T. Rueden *et al.*, ImageJ2: ImageJ for the next generation of scientific image data. *BMC Bioinformatics*. **18** (2017), doi:10.1186/s12859-017-1934-z.
46. E. F. Pettersen *et al.*, UCSF Chimera--a visualization system for exploratory research and analysis. *J. Comput. Chem.* **25**, 1605–1612 (2004).
47. A. Sorrentino *et al.*, MISTRAL: a transmission soft X-ray microscopy beamline for cryo nano-tomography of biological samples and magnetic domains imaging. *J. Synchrotron Radiat.* **22**, 1112–1117 (2015).
48. E. Pereiro, J. Nicolás, S. Ferrer, M. R. Howells, A soft X-ray beamline for transmission X-ray microscopy at ALBA. *J. Synchrotron Radiat.* **16**, 505–512 (2009).
49. G. Schneider *et al.*, Three-dimensional cellular ultrastructure resolved by X-ray microscopy. *Nat. Methods*. **7**, 985–987 (2010).
50. Y. Liu *et al.*, TXM-Wizard: a program for advanced data collection and evaluation in full-field transmission X-ray microscopy. *J. Synchrotron Radiat.* **19**, 281–287 (2012).
51. E. Beniash, R. A. Metzler, R. S. K. Lam, P. U. P. A. Gilbert, Transient amorphous calcium phosphate in forming enamel. *J. Struct. Biol.* **166**, 133–143 (2009).
52. D. Altamura *et al.*, X-ray microimaging laboratory (XMI-LAB). *J. Appl. Crystallogr.* **45**, 899 (2012).
53. T. Sibillano *et al.*, Interfibrillar packing of bovine cornea by table-top and synchrotron scanning SAXS microscopy. *J. Appl. Crystallogr.* **49**, 1231–1239 (2016).
54. D. Siliqi *et al.*, SUNBIM : a package for X-ray imaging of nano- and

biomaterials using SAXS, WAXS, GISAXS and GIWAXS techniques. *J. Appl. Crystallogr.* **49** (2016), doi:10.1107/S1600576716006932.
55. Altomare Angela *et al.*, QUALX2.0: a qualitative phase analysis software using the freely available database POW_COD. *J. Appl. Crystallogr.* **48**, 598–603 (2015).
56. M. F. Altaba, G. Tanelli, *Mineralogia* (Giunti Editore, 1994).
57. S. Boonrungsiman *et al.*, The role of intracellular calcium phosphate in osteoblast-mediated bone apatite formation. *Proc. Natl. Acad. Sci. U. S. A.* **109**, 14170–5 (2012).
58. Driessens F. C. M., Verbeeck R. M. H., Kiekens P., Mechanism of Substitution in Carbonated Apatites. *Z. Für Anorg. Allg. Chem.* **504**, 195–200 (1983).
59. N. Amizuka, T. Hasegawa, T. Yamamoto, K. Oda, [Microscopic aspects on biomineralization in bone]. *Clin. Calcium*. **24**, 203–214 (2014).
60. A. Bandyopadhyay, E. A. Withey, J. Moore, S. Bose, Influence of ZnO doping in calcium phosphate ceramics. *Mater. Sci. Eng. C*. **27**, 14–17 (2007).
61. A. Bigi, E. Foresti, M. Gandolfi, M. Gazzano, N. Roveri, Inhibiting effect of zinc on hydroxylapatite crystallization. *J. Inorg. Biochem.* **58**, 49–58 (1995).
62. T. J. Webster, C. Ergun, R. H. Doremus, R. Bizios, Hydroxylapatite with substituted magnesium, zinc, cadmium, and yttrium. II. Mechanisms of osteoblast adhesion. *J. Biomed. Mater. Res.* **59**, 312–317 (2002).
63. R. Lappalainen, M. Knuuttila, Atomic absorption spectrometric evidence of relationships between some cationic elements in human dentine. *Arch. Oral Biol.* **27**, 827–830 (1982).
64. H. Zhao, Membrane trafficking in osteoblasts and osteoclasts: new avenues for understanding and treating skeletal diseases. *Traffic Cph. Den.* **13**, 1307–1314 (2012).
65. F. Azari *et al.*, Intracellular precipitation of hydroxyapatite mineral and implications for pathologic calcification. *J. Struct. Biol.* **162**, 468–479 (2008).
66. M. E. Fleet, X. Liu, Calcium L2,3-edge XANES of carbonates, carbonate apatite, and oldhamite (CaS). *Am. Mineral.* **94**, 1235–1241 (2015).
67. F. De Groot, J. C. Fuggle, B. T. Thole, G. Sawatzky, L2,3 X-ray-absorption edges of d0 compounds: K+, Ca2+, Sc3+, and Ti4+ in Oh (octahedral) symmetry. *Phys. Rev. B Condens. Matter*. **41**, 928–937 (1990).
68. J. Cosmidis, K. Benzerara, N. Nassif, T. Tyliszczak, F. Bourdelle, Characterization of Ca-phosphate biological materials by scanning transmission X-ray microscopy (STXM) at the Ca L2,3-, P L2,3- and C K-edges. *Acta Biomater.* **12**, 260–269 (2015).
69. Y. Politi *et al.*, Transformation mechanism of amorphous calcium carbonate into calcite in the sea urchin larval spicule. *Proc. Natl. Acad. Sci. U. S. A.* **105**, 17362–17366 (2008).
70. S. Sviben *et al.*, A vacuole-like compartment concentrates a disordered calcium phase in a key coccolithophorid alga. *Nat. Commun.* **7**, 11228 (2016).
71. S. J. Naftel, T. K. Sham, Y. M. Yiu, B. W. Yates, Calcium L-edge XANES study of some calcium compounds. *J. Synchrotron Radiat.* **8**, 255–257 (2004).
72. A. R. Denton, N. W. Ashcroft, Vegard's law. *Phys. Rev. A*. **43**, 3161–3164 (1991).

73. C. Giannini, A. Fischer, C. Lange, K. Ploog, L. Tapfer, Heavy carbon doping of GaAs grown by solid-source molecular-beam epitaxy. *Appl. Phys. Lett.* **61**, 183–185 (1992).